CHALMERS

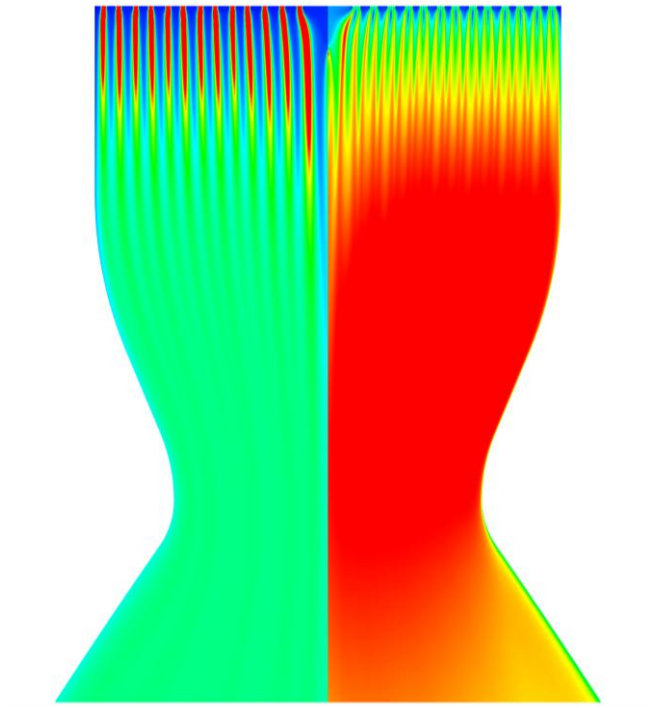

Simulation of flow and combustion in H2/O2 rocket thrust chambers using a 2D spray combustion method

Master's Thesis in the Master's Programme Applied Physics

ERIK LARSSON

Department of Applied Mechanics

Division of Fluid Mechanics

CHALMERS UNIVERSITY OF TECHNOLOGY

Göteborg, Sweden 2012

Master's thesis 2012:09

MASTER'S THESIS IN APPLIED PHYSICS

Simulation of flow and combustion in H2/O2 rocket thrust chambers using a 2D spray combustion method

ERIK LARSSON

Department of Applied Mechanics
Division of Fluid Mechanics
CHALMERS UNIVERSITY OF TECHNOLOGY
Göteborg, Sweden 2012

Simulation of flow and combustion in H2/O2 rocket thrust chambers
using a 2D spray combustion method

ERIK LARSSON

Master's Thesis 2012:09
ISSN 1652-8557
Department of Applied Mechanics

Division of Fluid Mechanics

Chalmers University of Technology
SE-412 96 Göteborg
Sweden
Telephone: + 46 (0)31-772 1000

Cover:
Figure of Vulcain 2 rocket thrust engine present in the main stage of Ariane 5. The left and right contour plots are showing the mixture ratio respectively temperature distributions. For more information see Figure 5.9 p. 49.

Department of Applied Mechanics
Göteborg, Sweden 2012

Simulation of flow and combustion in H2/O2 rocket thrust chambers
using a 2D spray combustion method

Master's Thesis in the *Master's Programme Applied Physics*

ERIK LARSSON
Department of Applied Mechanics
Division of Fluid Mechanics
Chalmers University of Technology

ABSTRACT

A new parameter setting to simulate H2/O2 rocket thrust chambers is found for the currently used two-dimensional, axisymmetric CFD-code Rocflam-II at Astrium GmbH in Ottobrunn, Germany. The generation program used for creating the necessary equilibrium lookup tables to the simulation is validated against an older version to make the generation for different fuel mixtures more consistent. Calculation of the isothermal compressibility of a multiple phase mixture is implemented together with unsuccessful measures to significantly decrease computational power. The program is also successfully modified to generalize the number of reaction products treated. The influence of the table resolution to Rocflam-II simulations is studied using the Vinci subscale thrust chamber. The study shows upon a possibility to slightly increase precision of the simulated rocket performance values by adjusting the mixture fraction resolution. The resolutions of the other parameters are found to be acceptable in their default settings. A formulation change is implemented in the Rocflam-II source to increase consistency between injected liquid droplets of different propellants. New correction functions for the droplet distribution for "warm" and "cold" injection of H2 are found using the CALO test case. The new correction functions and the Rocflam-II formulation change are applied to full-scale simulations of the Vulcain 2 rocket engine with good agreement to previous simulation results.

Contents

ABSTRACT I

CONTENTS II

PREFACE V

NOTATIONS VI

1 INTRODUCTION 1

2 THEORY 4

2.1 Rocket engines 4
2.2 Rocflam-II 6
2.2.1 Lagrange module 7
2.2.2 Droplet distribution 8
2.2.3 Lookup table 9
2.2.3.1 Interpolation 10
2.2.3.2 Integration 10
2.2.4 Compressibility coefficient 11
2.3 Thermodynamic property codes 12
2.3.1 CEA 12
2.3.2 GASPAK 13
2.4 Compressibility 13
2.5 CEA2FHR 16

3 CHANGES TO TABLE GENERATION SOFTWARE (CEA2FHR) 20

3.1 Validation 20
3.1.1 Simulation results 24
3.2 Common block coupling 24
3.2.1 Time aspect of table generation 25
3.3 Lifting of species limitation 26
3.4 Low temperature compressibility value 27
3.4.1 Simulation results 31

4 LOOKUP TABLE RESOLUTION STUDY 33

4.1 Test case: Vinci subscale 33
4.2 Resolution dependency 36

4.3 Recommendations regarding choosing table resolution 38
5 SIMULATION OF COMBUSTION CHAMBERS 40
5.1 CALO combustion chamber 40
5.2 Rocflam-II formulation change 42
5.3 Droplet distribution correction 43
5.4 CALO cold injection simulations 46
5.5 CALO warm injection simulations 47
5.6 Full scale simulation Vulcain 2 48
5.7 Discussion 51
6 CONCLUSION 54
REFERENCES 56
A CHANGE LIST FOR CEA2FHR 59

Preface

This master's thesis concludes the work carried out at the TP24 System Analysis department at Astrium GmbH in München during my employment as a master thesis worker from October 2011 to March 2012. The master's thesis is written within the Master's Programme Applied Physics at Chalmers University of Technology.

First and foremost I would like to thank my supervisors at Astrium, Björn Kniesner and Manuel Frey, for their guidance and helpfulness. I thank Ulf Palmnäs at Volvo Aero and Guenter Langel at Astrium that were instrumental in enabling me to find the position at Astrium. I would also like to thank my fellow interns and thesis workers at the department for help and the intensive language course. Moreover, I thank my supervisor and examiner Lars Davidson at the Department of Applied Mechanics for his assistance during my project.

München March 2012
Erik Larsson

Notations

Abbreviations

CEA	Chemical Equilibrium and Applications
CEA2FHR	CEA to mixture fraction (F) and relative enthalpy (HR)
GOX	Gaseous Oxygen
LOX	Liquid Oxygen
MMD	Mass Mean Diameter
PDF	Probability Density Function
PPDF	Presumed Probability Density Function
RCFS-II	Regenerative Coolant Flow Simulation, version II
Rocflam-II	Rocket Combustion Flow Analysis Module, version II
SIMPLE	Semi-Implicit Method for Pressure-Linked Equations
SMD	Sauter Mean Diameter

Roman letters

A_e, A_{th}	Exhaust/nozzle area, throat area
c^*	Characteristic exhaust velocity
c^*_{ideal}	Ideal exhaust velocity
c	Concentration Sound speed
c_{eff}	Effective exhaust velocity
C_{diff}	Rocflam-II diffusion coefficient
C_p	Heat capacity
C_ρ	Rocflam-II compressibility coefficient
$d_{Br,i}$	Coaxial injector fuel inner diameter
$d_{Br,a}$	Coaxial injector fuel outer diameter
d_{Ox}	Coaxial injector oxidizer diameter
D	Droplet diameter
D_{12}	Diffusion coefficient
dP	Pressure drop of coolant flow
$\mathrm{E}(D)$	Expectancy value
f	Mixture fraction

F	Thrust
g	Earth acceleration
g_f	Mixture fracture variance
$\tilde{h}$	Static enthalpy
h_{sec}	Secondary injection enthalpy
h_{prim}	Primary injection enthalpy
$\mathrm{h_Q}$	Relative enthalpy
h_{inj}	Injection enthalpy
i	Lookup table index
I_0, I_1	Gaussian tails
I_{sp}	Specific impulse
J	Molar flux
k	Turbulent kinetic energy
$\dot{m}$	Mass flow
M_t	Total molar mass
O/F	Oxidizer to fuel ratio
p	Pressure
p_c	Chamber pressure
p_e	Pressure exhaust
P	Probability density function
$\dot{q}_w$	Specific wall heat flux
$\dot{Q}_w$	Integral heat load
	Recess in coaxial injector
R	Rest in index calculation
	Ideal gas constant
T	Temperature
T_{ad}	Temperature with adiabatic conditions
v	Velocity
v_e	Average exhaust velocity
V	Volume
V_r	Relative velocity
y	Correction factor

Greek letters

α	Heat transfer coefficient
β_T	Isothermal compressibility
γ	Adiabatic index
ε	Turbulent dissipation rate
η_{c^*}	Combustion efficiency
λ	Heat conductivity
μ	Gaussian distribution displacement parameter Viscosity
μ_e	Effective viscosity
ξ	Mass fraction
ρ	Density
σ	Log-normal distribution shape parameter
Φ	Lookup table variable
ψ	Mole fraction

Subscripts

$corr$	Corrected
f	Fuel
g	Gas
i	Lookup table specie
l	Liquid
Ox	Oxidizer
s	Solid
w	Wall

Superscripts

$'$	Correction (prim)

1 Introduction

On the 23rd of March 2012 an Ariane 5 ES launch system lifted the third Automated Transfer Vehicle "Edoardo Amaldi" to the International Space Station propelling a payload of 20.1 tons [**1**]. The main core stage of the launch system contains the cryogenic H2/O2 engine Vulcain 2. The Vulcain 2 provides 1 350 kN of vacuum thrust, 20% more than its predecessor [**2**].

The simulation of flow and combustion in a combustion chamber has become an essential part of the design process for a rocket engine. With advancing simulation capabilities more and more of possible causes of failures can be found and disabled before spending large sums on construction, testing and failed missions. As one of the main contractors of the Vulcain 2 engine Astrium is using various tools to simulate the flow and combustion inside the thrust chamber. One of these tools is the self-developed multi-phase finite volume code Rocflam-II [**3**].

For flow simulations of cryogenic H2/O2 rocket combustion chambers using Rocflam-II information is needed regarding the combustion between the two propellants hydrogen (H2) and liquid oxygen (LOX), which the CFD code draws from a lookup table. To generate this table Astrium has developed a table generation program called CEA2FHR that to a large extent automatizes the process of generating the required lookup table.

In an earlier work by Martin Merkle [**4**] the table generation software was adapted to include low temperature regions of a lookup table generated for a Methane-LOX combustion mixture. After this change to the framework of the program a validation of the H2-LOX mixture application was needed to consolidate the two versions of the program. The new framework also incurs a considerable increase in the generation time of a typical table. To increase the time efficiency a direct coupling of the main subroutine common blocks to the main program was proposed. A problem with the program at this point was also that only twelve product species could be simulated for a given combustion mixture. For a combustion mixture of, for example, Kerosene-GOX (gaseous oxygen) this becomes a problem since many different combustion products are formed depending on the type of combustion.

Since the simulation uses the table as a critical data source, not just the accuracy of the actual values in the lookup table is important. A main factor in the precision of the

simulation is how well the discretized tables describe the continuous functions the simulation seeks. Because the time for generating large lookup tables can be in the order of days, the resolution needs to be optimized to see where corners can be cut without losing precision. A simple study of the "convergence" to similar temperatures in simulation depending on the table resolution was performed in [**5**] but until now no comprehensive study of the table resolution influence has been made at Astrium.

Another issue regarding the lookup table is the approximation of the mixture compressibility (for definition see Section 2.4). In high temperature regions ($\gtrsim$ 800 K) a good approximation of this value is given by an ideal gas assumption. For lower temperatures ($\lesssim$ 400 K), where phase transitions occur of the included product species, this is no longer the case. The current table generation software uses the ideal gas assumption in both regions and does not consider the effects of the condensed phases to the compressibility value. Since the condensed phases have a nearly incompressible behavior compared to the gas phases the total compressibility is expected to decrease with increasing mass fraction of the condensed phases in the equilibrium mixture.

The current formulation of the Rocflam-II source code has inconsistencies in treating the injection of H2/O2 compared to other types of fuel mixtures. In [**6**] a new value for the diffusion coefficient in the simulation was proposed that would enable removing the special treatment of the H2/O2 mixtures and improve consistency and transparency of the source code.

The purpose of this thesis is to describe and solve the current problems with the table generation software at Astrium. The influence of the lookup table resolution to the simulations shall also be studied. Finally this thesis seeks to validate a new formulation of the Rocflam-II source and apply these settings to the simulation of the Vulcain 2 and CALO rocket engines. The thesis is limited to the problems of the table generation program when generating H2/O2 tables and only considering one rocket engine when investigating the influence of the lookup table resolution. The validation and implementation of the new formulation will be limited to the two H2/O2 engines mentioned above.

The problems with the current table generation software version are solved through investigations into literature and the source code of the program. For the table resolution study the Vinci subscale combustion chamber is chosen as a test case for simulations. Validation of the lookup table software is made by comparing typical output lookup tables and analyzing the underlying calculation routines. The formulation change to

increase the Rocflam-II consistency is investigated on the CALO test case and a full scale Vulcain 2 simulation.

In this thesis a short theoretical background of rocket engines and the tools used in simulating these is given in Chapter 2. The changes to the table generation software are then described in Chapter 3 together with the results and discussion of these changes. In Chapter 4, the lookup table resolution study is described and the results presented. The formulation change to Rocflam-II and the simulations are presented in Chapter 5. Finally the conclusion of the thesis is given in Chapter 6.

2 Theory

2.1 Rocket engines

A schematic figure of a typical cryogenic rocket combustion chamber can be seen in Figure 2.1 below. The injector elements are attached to the face plate where they inject fuel and oxidizer into the combustion chamber. The mixture combusts and exists the chamber through the throat into the nozzle.

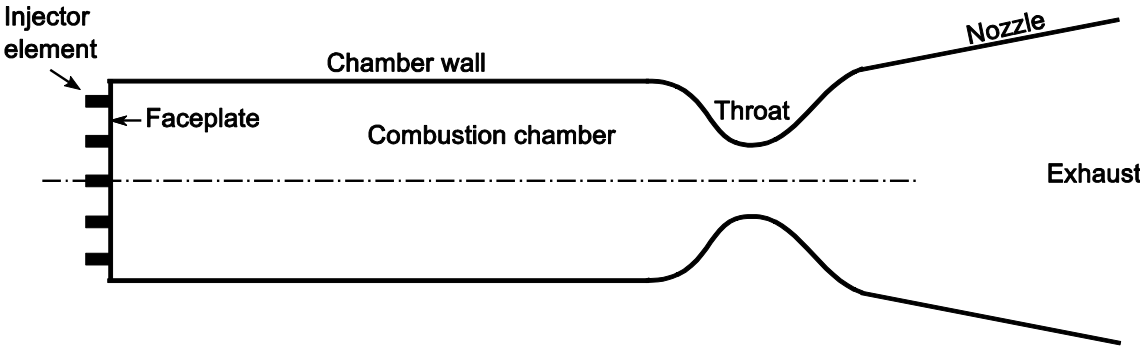

Figure 2.1: Schematic figure of a cryogenic rocket thrust chamber with attached nozzle.

The main purpose of a rocket engine is to provide thrust to a rocket that is to be accelerated. The thrust F can be described as

$$F = \dot{m}v_e + (p_e - p_a)A_e \tag{2.1}$$

The first term of the thrust is due to the momentum given by the total mass flow $\dot{m}$ exiting the rocket with an average velocity v_e [7]. The second term is due to the pressure difference between the gases exiting the rocket through the nozzle exit area A_e with pressure p_e and the ambient pressure p_a. Through the definition of the effective exhaust velocity c_{eff} both terms can be described by one constant and the equation simplifies to

$$F = \dot{m}c_{eff} \tag{2.2}$$

The thrust can then be increased by either optimizing for the effective exhaust velocity or simply increasing the amount of fuel ejected from the rocket by increasing $\dot{m}$. A higher c_{eff} enables the rocket to carry less fuel and a heavier payload. To describe this in forms of a performance parameter the specific impulse I_{sp} is defined as

$$I_{sp} = \frac{F}{\dot{m}g} = \frac{c_{eff}}{g} \tag{2.3}$$

with g being the earth acceleration. The specific impulse can be thought of as the amount of thrust produced from a certain fuel mass flow.

In chemical rocket engines the characteristic exhaust velocity c^* is also used to compare performance of different fuel mixtures and engine designs [**7**]. It is defined as (2.4) where p_c is the chamber pressure and A_{th} being the cross section area of the chamber throat.

$$c^* = \frac{p_c A_{th}}{\dot{m}} \tag{2.4}$$

The characteristic exhaust velocity acts as a measure of the efficiency of the combustion in the chamber. By an imperfect combustion the highest possible pressure is not reached in the chamber and c^* is smaller than its theoretical maximum c^*_{ideal}. Through equilibrium computation c^*_{ideal} is calculated where it is assumed that the propellants go through an ideal isentropic expansion. The combustion efficiency of the rocket engine is calculated through the ratio of these values as

$$\eta_{c^*} = \frac{c^*}{c^*_{ideal}} \tag{2.5}$$

The fuel and oxidizer injected in the chamber for a H2/O2 engine combust at a temperature value much higher than the melting points of the materials from which the chamber wall is constructed. Active cooling systems are therefore often incorporated into the chamber and nozzle. To investigate the need for cooling the specific wall heat flux $\dot{q}_w$ is formed and computed through

$$\dot{q}_w = \alpha(T_{ad} - T_w) \tag{2.6}$$

α being the heat transfer coefficient of the wall material which can be determined through experiment or CFD simulations. T_{ad} is the wall temperature from a simulation with adiabatic boundary conditions ($\dot{q} = 0$) and T_w is the actual wall temperature. The integral heat load of the chamber wall $\dot{Q}_w$ can be calculated by integrating the specific wall heat flux over the wall area (2.7). The load can be measured in experiments through the temperature of the cooling medium.

$$\dot{Q}_w = \int_A \dot{q}_w \, dA \tag{2.7}$$

The propellants for H2/O2 rocket engines treated in this thesis are injected through coaxial injection elements which are composed by a central injection of a liquid or transcritical oxidizer surrounded by a gas stream of fuel. The central oxidizer stream has a far lower exit velocity than the surrounding fuel stream and droplets break off from the oxidizer stream in the shear layer between them to form a spray into the chamber. A typical coaxial element and the presumed break up are shown in Figure 2.2. The H2 gas stream (2) is limited by $d_{Br,i}$ and $d_{Br,a}$ and the oxidizer stream (1) diameter is controlled by d_{Ox}. The recess R indicates the distance from the end of the oxidizer lip to the faceplate.

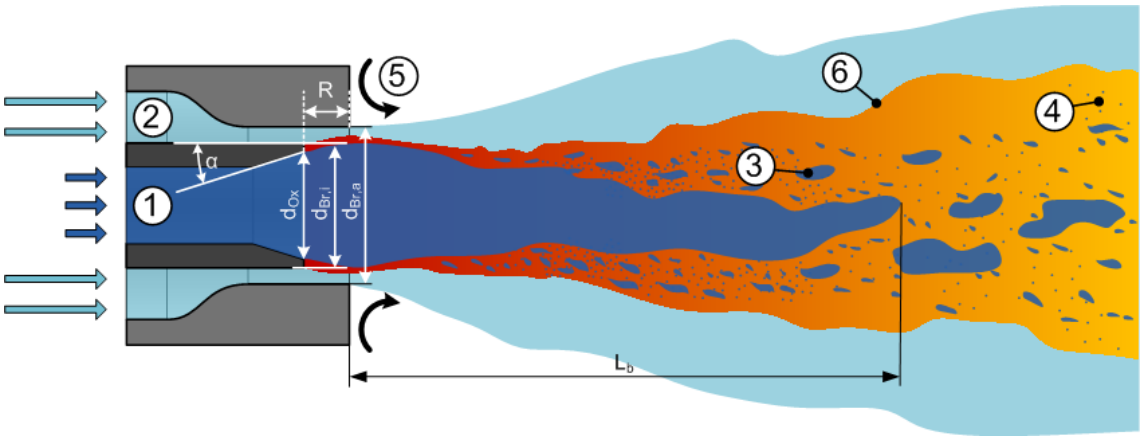

*Figure 2.2: A coaxial injection element with a central oxidizer stream (1) surrounded by a fuel gas stream (2), from [**8**].*

2.2 Rocflam-II

Rocflam-II (Rocket Combustion Flow Analysis Module, version II) is a Navier-Stokes code developed by Astrium Space Transportation to analyze combustion and flow in rocket thrust chambers [**3**]. The finite volume code solves the Favre-averaged fluid flow equation on a discretized 2D axisymmetric numerical grid. Since the grid is axisymmetric all 3D effects of the thrust chamber are neglected, leading to a lower accuracy in the very front of the chamber close to the asymmetric face plate. The set of equations for the mass, momentum, energy, and, if needed, species or mixture fraction are solved by an implicit algorithm. The turbulence is modeled through a $k-\varepsilon$ approach, modified for a compressible flow, where the turbulent kinetic energy k and turbulent dissipation rate ε are solved through transport equations [**9**]. Modeling of the

wall region is made by either a logarithmic or two-layer approach. To account for the combustion two different chemical reaction models can be chosen: A multi-step global reaction scheme or a PPDF (Presumed Probability Density Function) of tabulated equilibrium chemistry. Through inclusion of the Astrium developed RCFS-II (Regenerative Coolant Flow Simulation, version II) routine the simulation can also be coupled with an active cooling system of the combustion chamber wall.

2.2.1 Lagrange module

In addition to solving the transport equations of the gas phase Rocflam-II can also simulate multiple droplets in a Lagrangian reference frame. This is used to simulate propellants of different sizes in condensed phase being dispersed, or "sprayed", into the gas phase. In this reference frame the droplet trajectories are calculated by integrating the force balance resulting from the interaction with the gas phase, the wall and themselves.

The droplets are divided into discrete packages to increase calculation efficiency and are sequentially injected into the combustion chamber. A droplet in condensed phase being injected into the chamber is heated by the surrounding gas phase continuously along its trajectory. With help of a binary diffusion reaction the gas phase is assigned source terms for mass, impulse and energy along the trajectory until the droplet is entirely vaporized. For a gas phase droplet the entire source terms are added to the cell where the droplet originates. The reaction is described by (2.8) where the temperature and pressure dependence is modeled through the diffusion coefficient D_{12}. In Rocflam-II the rate of the diffusion is controlled by the parameter C_{diff} that enters as a constant in the expression for D_{12}, also dependent on the temperature T and pressure p [**10**].

$$J_1 = -D_{12}\frac{dc_1}{dz} \qquad D_{12} = C_{diff}\frac{T^{1.75}}{p} \tag{2.8}$$

In (2.8) J_1 is the molar flux of the diffusing specie and dc_1/dz the concentration gradient of the diffusing species between the droplet atmosphere and the surrounding gas phase. In Rocflam-II there is also support for a one-dimensional model of liquid film cooling for the combustion chamber. The model describes the film through the build-up of condensed phase droplets aggregating on the wall and the gas-film-wall heat transfer.

2.2.2 Droplet distribution

The droplets are distributed into discrete packages over a corrected log-normal distribution described in [**5**]. The droplets are divided into different diameter classes with a specific probability to be injected into the combustion chamber. Due to computational reasons the number of classes is limited to ten. The shape parameter σ of the log-normal distribution and the expectancy value $\mathrm{E}(D)$, where D being the droplet diameter, are used to control distribution through Rocflam-II inputs. When adapting the droplet distribution to the different load points and injection conditions the expectancy value is varied and the MMD (Mass Mean Diameter) is used as a physical interpretation of $\mathrm{E}(D)$. MMD represent the diameter where half of the total mass of injected droplets has a diameter smaller than the MMD. The effect of varying the expectancy value to the log-normal distribution can be seen in the left part of Figure 2.3. The shape parameter controls the "width" of the distribution with higher σ meaning a greater width, as seen in the left part of Figure 2.3. Because of the greater width it also increases the MMD of the distribution.

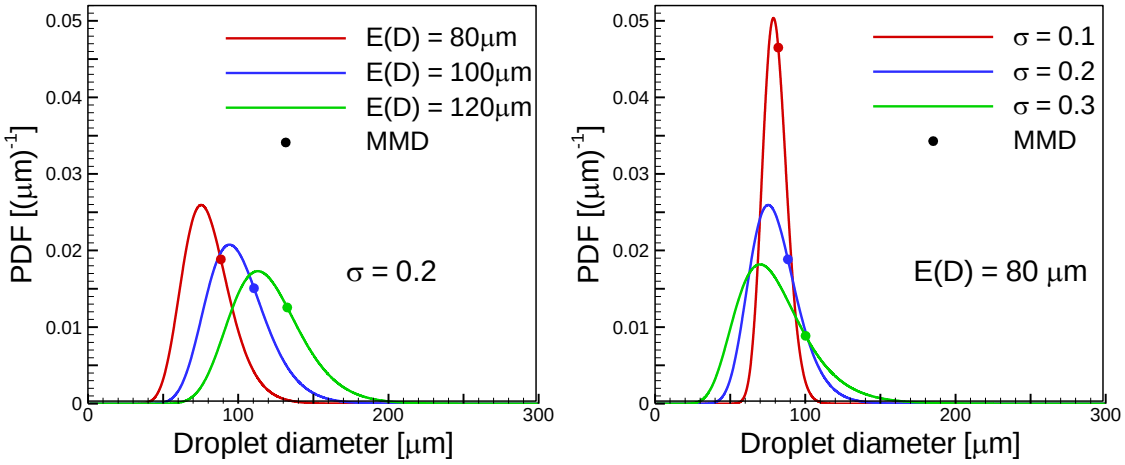

Figure 2.3: Figures showing the effect of changing the expectancy value $E(D)$ and the shape parameter σ to the log-normal droplet probability density function (PDF). The MMD is marked by the filled circles for each of the distributions.

Investigations into the shape of the droplet distribution exist in literature. In [**11**] injection elements, similar to the ones used in the Vinci subscale and CALO combustion chamber, were used to investigate the droplet distribution in experiments with water and helium as substitutes for LOX respectively H2. From these investigations two empirical formulas (2.9) and (2.10) are proposed to estimate the Sauter Mean Diameter (SMD). The SMD is defined as the diameter of a droplet with the same volume to surface area as the entire droplet distribution. The geometrical

parameters of the coaxial injection element are defined in Figure 2.2. V_r is the relative velocity between the oxidizer and fuel streams.

$$SMD = 127 \cdot \left(\frac{V_r}{160}\right)^{-0.93} \left(\frac{d_{Ox}}{2}\right)^{2.25} \left(\frac{d_{Br,a}}{3}\right)^{-2.65} \left(\frac{R}{d_{Ox}}\right)^{-0.26} \tag{2.9}$$

$$SMD = 5.68 \cdot 10^4 (V_r)^{-0.9} (d_{Ox})^{2.2} \left(d_{Br,a}\right)^{-2.7} \left(\frac{R}{d_{Ox}}\right)^{-0.25} \tag{2.10}$$

The SMD can easily be expressed in forms of MMD through the log-normal distribution by (2.11) [**8**].

$$MMD = SMD \cdot e^{0.5\sigma^2} \tag{2.11}$$

2.2.3 Lookup table

When using the PPDF combustion model a lookup table containing the equilibrium values for a given mixture fraction f, relative enthalpy h_Q, and pressure p must be provided. The relative enthalpy describes the change in absolute enthalpy from the injection enthalpy and can be calculated through the static enthalpy $\tilde{h}$, the "primary" droplet injection enthalpy h_{prim} and the "secondary" droplet injection enthalpy h_{sec} as

$$h_Q = \tilde{h} - [f h_{prim} + (1 - f) h_{sec}] \tag{2.12}$$

The mixture fraction in turn is defined as the fraction of the fuel mass flow $\dot{m}_f$ and sum of the total fuel and oxidizer mass flow (2.13). The fraction can also be described as a mixture ratio between the oxidizer and fuel mass flow, named O/F.

$$f = \frac{\dot{m}_f}{\dot{m}_f + \dot{m}_{ox}} = \frac{1}{O/F + 1} \tag{2.13}$$

These three variables completely define the thermodynamic state and are therefore seen as the independent state variables of the table. Each set of the state variables is paired together with a list of thermodynamic properties (see Table 2.1), for example the temperature, describing the state. Mathematically this is expressed as

$$\Phi = \Phi(f, h_Q, p) \tag{2.14}$$

with Φ being the set of properties. The value of f, p, and h_Q are given by the normal transport equations in the gas phase solver of Rocflam-II. From these variables the required values can be found by making a table lookup and interpolating between the eight closest points in the three dimensional array made up of the independent variables. Each of the properties in the list is in this way interpolated and extracted for use in the simulation routine.

2.2.3.1 Interpolation

For each of the state variables the index i and remainder R of the position in the table array are calculated. For the enthalpy variable the expression is as follows [**10**].

$$\begin{aligned} i_{h_Q} &= integer\left[\left(h_Q - h_{Q\,min}\right)/\left(h_{Q\,max} - h_{Q\,min}\right)\right] + 1 \\ R_{h_Q} &= \left(h_Q - h_{Q\,min}\right)/\left(h_{Q\,max} - h_{Q\,min}\right) + 1 - i_{h_Q} \end{aligned} \tag{2.15}$$

For an interpolation in only the enthalpy dimension the formula for the list variables becomes

$$\Phi\left(i_f, h_q, i_p\right) = R \cdot \Phi\left(i_f, i_{h_Q}, i_p\right) + (1 - R) \cdot \Phi\left(i_f, i_{h_Q} + 1, i_p\right) \tag{2.16}$$

The index and remainder is calculated for each state variable and the list value can be found by interpolating over the eight points created by the permutation of the two neighboring indices of each state variable. The process can be visualized by thinking of it as interpolating a point inside a cube where the eight corners represent the points to interpolate from.

2.2.3.2 Integration

The PPDF modeling includes the variance of the mixture fraction g_f to simulate the influence of the turbulence to the equilibrium chemistry. The variance describes the width of the mixture fraction distribution. With a large measure of turbulence the mixture fraction can be assumed to vary further from its average, thus having a bigger variance. The variance is determined through an additional transport equation and enters as a parameter into the PPDF. When having the full set of parameters needed for the PPDF the values of the properties Φ under the distribution can be computed through integration. The PPDF $P(f)$ is often chosen as a clipped Gaussian or beta distribution.

In the case of the clipped Gaussian the two tails (I_0, I_1) are added to the integration over the domain of f as in (2.17).

$$\Phi(f, g_f) = \int_{0+}^{1-} \Phi(f) P(f, g_f) df + I_0 \Phi(f = 0) + I_1 \Phi(f = 1) \qquad (2.17)$$

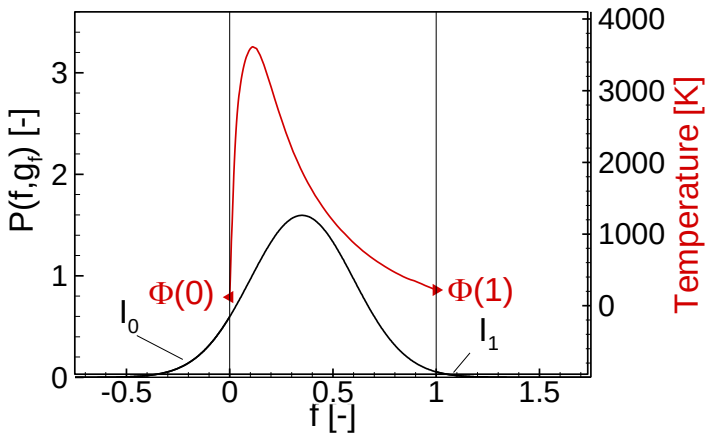

Figure 2.4: Here a Gaussian distribution with μ 0.35 (f) and σ 0.25 (g_f) is shown together with the temperature Φ over the range $f = [0,1]$, with the two tails I_0 and I_1 shown outside this range. The variance of the distribution is exaggerated, compared to typical values in simulation ($g_f \approx 10^{-5}$), to show the tails more clearly.

2.2.4 Compressibility coefficient

The Rocflam-II code uses the SIMPLE (Semi-Implicit Method for Pressure-Linked Equations) algorithm to solve the Navier-Stokes equations [**10**]. The SIMPLE algorithm works by firstly solving the momentum equation for the velocities using a guessed pressure field taken from the previous pressure distribution or an initial guess. The pressure correction equation is then solved with the uncorrected velocity field to yield the corrected pressure distribution. After this step the velocities are corrected using the new pressure distribution and a set of mass flux corrections are calculated from the corrected velocity field [**12**].

In compressible flows the mass flux correction is not only dependent on the velocity but also on the variable density of the fluid [**13**]. If the SIMPLE method is to work in the compressible case the density correction must be expressed in terms of the pressure correction. If the temperature is assumed to be constant for one of these correction steps the density correction ρ' can be described in terms of the pressure correction p' as

$$\rho' \approx \left(\frac{\partial \rho}{\partial p}\right)_T p' \stackrel{\text{def}}{=} C_\rho p' \tag{2.18}$$

For nearly ideal gases the value of the compressibility coefficient C_ρ can be drawn from the ideal gas law (2.21) but must be calculated for any other types of mixture as described in Section 2.2.4. The converged solution is independent of C_ρ since all corrections at this point ideally are zero [**13**]. The coefficient can however influence the convergence behavior for a more complex system where different systems interact to achieve convergence. An example of this for Rocflam-II can be seen in Figure 3.7.

2.3 Thermodynamic property codes

Two different thermodynamic property codes, CEA and GASPAK, are used to generate the lookup table for the H2-LOX mixture. By combining the two codes, tables with temperatures down to 60 K can be generated. A short background for these programs are given below.

2.3.1 CEA

The CEA software (Computer Program for Calculation of Complex Chemical Equilibrium Compositions and Applications) was developed by Sanford Gordon and Bonnie J. McBride while working for NASA [**14**]. The program solved the problem of getting good estimates for many different kinds of chemical equilibriums, together with some applications in the problems faced by the space program. The program includes a number of application modules with *THERMP* being the main one for equilibrium problems. The module computes the equilibrium by iteratively minimizing the Gibbs free energy (2.19) for a mixture of ideal gases and pure condensed species.

$$g = \sum_{j=1}^{N} \mu_j n_j \qquad \mu_j = \left(\frac{\partial g}{\partial n_j}\right)_{T,P,n_{i\neq j}} \tag{2.19}$$

The *THERMP* module has support for both solid and fluid species which has to be specified to be part of the mixture a priori. The most current version of the program was published 1994 (with the latest update in 2004) and contains numerous improvements to the earlier version, published in 1976. For generating solutions to an enthalpy-pressure (*hp*) problem the user specifies an input file where the enthalpy, pressure and proportion

of the original mixture are specified together with the products after the reaction. When the main program is called it interprets the input file and runs the main module *THERMP* to find the equilibrium point. The result is written directly to an output file in a format specified in the input file.

2.3.2 GASPAK

GASPAK was developed by Vincent Arp, Bob McCarty, and Jeff Fox of Cryodata based upon an earlier code called MIPROPS, published by the National Institute of Standards and Technology [**15**]. This program computes the properties for fluids by using fundamental state equations that are defined by a set of coefficients. From these equations can the needed properties be computed. The coefficients for the equations are read from specie property files that are provided together with the program. The program output presents together with the computed properties whether each of the species exists in a fluid or gaseous state.

2.4 Compressibility

Compressibility is in thermodynamics and fluid mechanics defined as a measure of the relative volume change of a fluid or solid to a pressure change [**16**]. The compressibility can also be described in terms of the density and for the definition to be complete the process needs to be defined as either adiabatic or isothermal. For reason described in Section 2.2.4 the definition is here chosen as isothermal. In the applications within this thesis it is assumed that the different species are "frozen" in equilibrium, this corresponding to the individual mass fractions ξ_i remaining constant after the equilibrium calculations. This assumption interprets to the pressure change applied to the mixture not causing any phase transition in the mixture. For the purpose of this thesis the isothermal compressibility is from [**16**] redefined in terms of density as (2.20).

$$\beta_T = -\frac{1}{V}\left(\frac{\partial V}{\partial p}\right)_T = \frac{1}{\rho}\left(\frac{\partial \rho}{\partial p}\right)_T \tag{2.20}$$

From the ideal gas law the ideal gas approximation of the isothermal compressibility can be written as (2.21).

$$\beta_T = \frac{1}{\rho}\left(\frac{\partial \rho}{\partial p}\right)_T = \frac{1}{\rho}\,\frac{1}{RT} \tag{2.21}$$

For reasons associated with the simulation (see Section 2.2.4) the required value is the absolute instead of the relative density change to the pressure. We define this value as the compressibility coefficient C_ρ (2.22).

$$C_\rho \overset{\text{def}}{=} \left(\frac{\partial \rho}{\partial p}\right)_T \tag{2.22}$$

In the case of H2/O2 combustion the main product is water that in the temperatures ranges present in the combustion chamber can exist in its three main phases: Ice, water, and steam. The compressibility of these three phases is very different. Ice and water can be thought of as nearly incompressible and steam as an ideal gas, at least for high temperatures. To determine the value of $\partial\rho/\partial p$ for the mixture of two or three phases a mixing rule for this quantity must be derived.

To derive an equation for the change of density dependent on pressure we assume a gas-liquid mix. The gas consists after combustion, if we are close to stoichiometric fraction in the mixture, mostly of gaseous water and residual gas, either fuel (H2) or oxidizer (O2). Since more than one type of gas is present a relation for the total compressibility of the gas phase is needed. For the gas phase the partial densities are provided from the computation of the gas state using the partial instead of the total pressure. The density of the total gas mixture ρ_g and the partial pressure p_i can be expressed as (2.23), where N_g gas species are summated and ψ_i is the mole fraction of each gas specie i.

$$\rho_g = \sum_i^{N_g} \rho_i \qquad\qquad p_i = \psi_i p \tag{2.23}$$

By using the chain rule the expression for the desired pressure derivative can be constructed.

$$\frac{\partial \rho_g}{\partial p} = \sum^{i} \frac{\partial p_i}{\partial p}\frac{\partial \rho_i}{\partial p_i} \tag{2.24}$$

The derivative $\partial\rho_i/\partial p_i$ is given for the different gas species through the calculation with the partial pressure. $\partial p_i/\partial p$ is given through the expression for the partial pressures so that the final expression for the gas part differential becomes (2.25).

$$\frac{\partial \rho_g}{\partial p} = \sum^{i} \psi_i \frac{\partial \rho_i}{\partial p_i} \tag{2.25}$$

With the expressions for the gas phase finished the multiphase system as a whole is studied. For two present phases the total density is formed by reciprocal summation, weighted with the respective mass fractions as in (2.26).

$$\rho = \left(\frac{\xi_g}{\rho_g} + \frac{\xi_l}{\rho_l} \right)^{-1} \tag{2.26}$$

Here the subscript of the variables mass fraction ξ and density (ρ) indicates the gaseous (g) or liquid (l) phase. By using the chain rule once more an expression for the searched after differential can be found.

$$\frac{\partial \rho}{\partial p} = \frac{\partial \rho}{\partial \rho_g} \frac{\partial \rho_g}{\partial p} + \frac{\partial \rho}{\partial \rho_l} \frac{\partial \rho_l}{\partial p} \tag{2.27}$$

The value of $\partial \rho_g / \partial p$ is taken from the value for the total gas mixture (2.25) and $\partial \rho_l / \partial p$ from the value of the liquid specie, in our case water. The other derivatives can be computed from equation (2.26) and by using an analog derivation to the one above for a three phase mixture the equation (2.27) can be expanded to encompass all of the available phases.

$$\frac{\partial \rho}{\partial p} = \frac{\frac{\xi_g}{\rho_g^2} \frac{\partial \rho_g}{\partial p} + \frac{\xi_l}{\rho_l^2} \frac{\partial \rho_l}{\partial p} + \frac{\xi_s}{\rho_s^2} \frac{\partial \rho_s}{\partial p}}{\left(\frac{\xi_g}{\rho_g} + \frac{\xi_l}{\rho_l} + \frac{\xi_s}{\rho_s} \right)^2} \tag{2.28}$$

The definition of the speed of sound in a medium is very similar to the calculated value above. For an adiabatic and reversible crossing of the sound wave the following expression holds for the sound speed c [**16**].

$$c^2 = \left(\frac{\partial p}{\partial \rho} \right)_s \tag{2.29}$$

This expression is close to the value defined for compressibility coefficient above. Here is the inverse of the differential taken at isentropic instead of isothermal conditions. For

an ideal gas the differential taken at isothermal conditions differs from the isentropic one with the factor $\sqrt{\gamma}$, with γ being the adiabatic index (or ratio of specific heats). The value of C_ρ could therefore also be used to compute the speed of sound for a mixture where the ideal gas approximation holds.

2.5 CEA2FHR

The table generation program CEA2FHR (CEA to mixture fraction (F) and relative enthalpy (HR)) is used to create a table of thermodynamic and transportation properties of a combustion mixture. The generated data is used as a lookup table in the Rocflam-II simulations. The simulation routine defines a state point by pressure, enthalpy and mixing factor from which the table shall provide corresponding properties.

The table is therefore generated, in order, over pressure, enthalpy, and mixing factor. For each of these entries the properties shown in Table 2.1 are calculated for the mixture. The mass fractions of each of the N species are also presented in the generated table.

Table 2.1: Properties calculated for the combustion mixture and provided in the lookup table.

Property	**Symbol**	**Unit**
Temperature	T	K
Total molar mass	M_t	mol/kg
Density	ρ	kg/m^3
Inverse of compressibility coefficient	$(\partial p/\partial \rho)_T$, $(C_\rho)^{-1}$	m^2/s^2
Heat capacity	C_p	J/(kg K)
Viscosity	μ	Pa s
Heat conductivity	λ	W/(m K)
Mass fractions	$\xi_i \quad i = 1,2,3 \ldots N$	-

The table can be visualized by imagining the look-up state points distributed in a cube where each axis represent one of the state point variables. Each of these state points in the cube mesh contains a dataset of the properties listed in Table 2.1.

The calculations are done by calling the CEA program for a specified state point, pressure enthalpy, and mixture fraction, and then formatting the results to the desired format. For a CEA *hp*-problem the presence of condensed species is not known a priori. This together with the ideal gas modeling makes the program unsuitable for calculations

in low temperature and mixed phase regions. To overcome this limitation of CEA the GASPAK program is tied in to find the thermodynamic properties. To create a smooth transition between the ranges of the different program the values are linearly interpolated between an upper and a lower transition temperature. This means that for computed combustion mixture temperatures of CEA below the transition temperature a part or all of the data for the computed thermodynamic properties are drawn from GASPAK calls. For tables with H2/O2 combustion mixtures 800 and 1000 Kelvin are usually chosen as the lower respectively higher limit for the interpolation region (see Figure 2.5).

The GASPAK routine does not contain any method to compute the equilibrium of a given multi species mixture. To find the equilibrium distribution of species in the low temperature range the CEA solution is used for all state points where this exists. For temperatures where the CEA solution is not available the enthalpy is raised in small increments until a valid solution is found. For H2/O2 tables the possible products for lower temperatures are H2O together with a residual gas depending on if the mixture is oxidizer or fuel rich. For temperatures under the limit of CEA it is assumed that the mass proportions of the equilibrium mixtures remains constant and does not change significantly.

The temperature is solved using the mass proportions from the CEA call for the low temperature mixture. An iterative approach is applied where the temperature is optimized by the secant method to match the desired enthalpy and to compute the correct thermodynamic properties. For very low enthalpies the routine fails to find a solution usually because the low temperature is outside the range of GASPAK for one of the species. For this reason a minimum temperature of 60 K has been given as the lowest allowed temperature in the table. Every solution under this limit is rejected by the low temperature subroutine and not displayed in the final output table. Because of reasons due to the integration in Rocflam-II the empty solution spots in the state point mesh is filled with the closest “found” solution of higher enthalpy. This “fill-up” region consists of properties for the corresponding mixture at approximately 60 K.

In Figure 2.5 the different regions of a typical H2/O2 table for fixed pressure are shown with the corresponding isotherms marked. The stoichiometric mixture fraction ($f = 0.11189$) and the injection enthalpy h_{inj} ($h_Q = 0$) are also indicated in the figure.

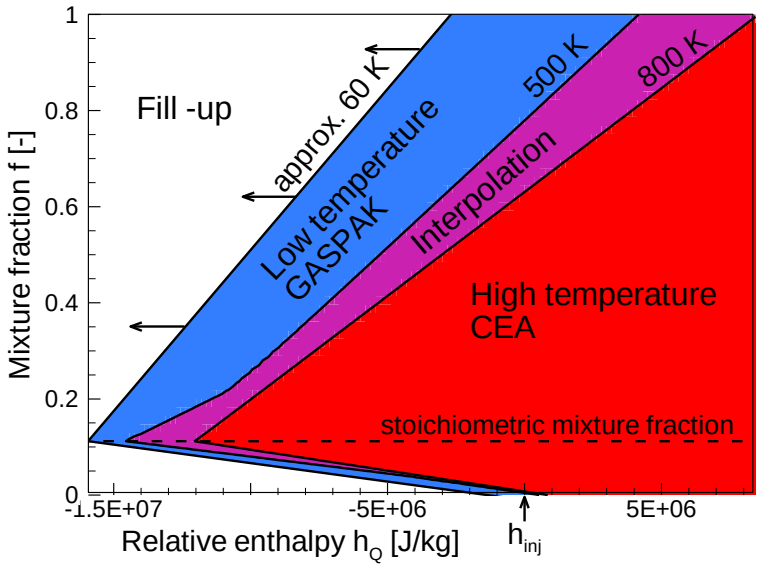

Figure 2.5: View of a typical H2/O2 lookup table with the different computing regions indicated. The limit of 60 K is introduced to avoid range problems of GASPAK and is for reasons due to Rocflam-II integration filled with the closest "found" solution of higher enthalpy. The isotherms are plotted for a fixed pressure of 60 bar.

In Figure 2.6 the temperature is plotted over f and h_Q for the same table at a fixed pressure of 60 bar. The white line indicates the stoichiometry of the combustion mixture showing the temperature maximum for the corresponding enthalpy value. The influence of the pressure can be seen in the upper left corner of the figure where corresponding temperatures for 0.1 bar can be seen. The two fill-up regions are also marked where temperature is "filled up" from a higher enthalpy level.

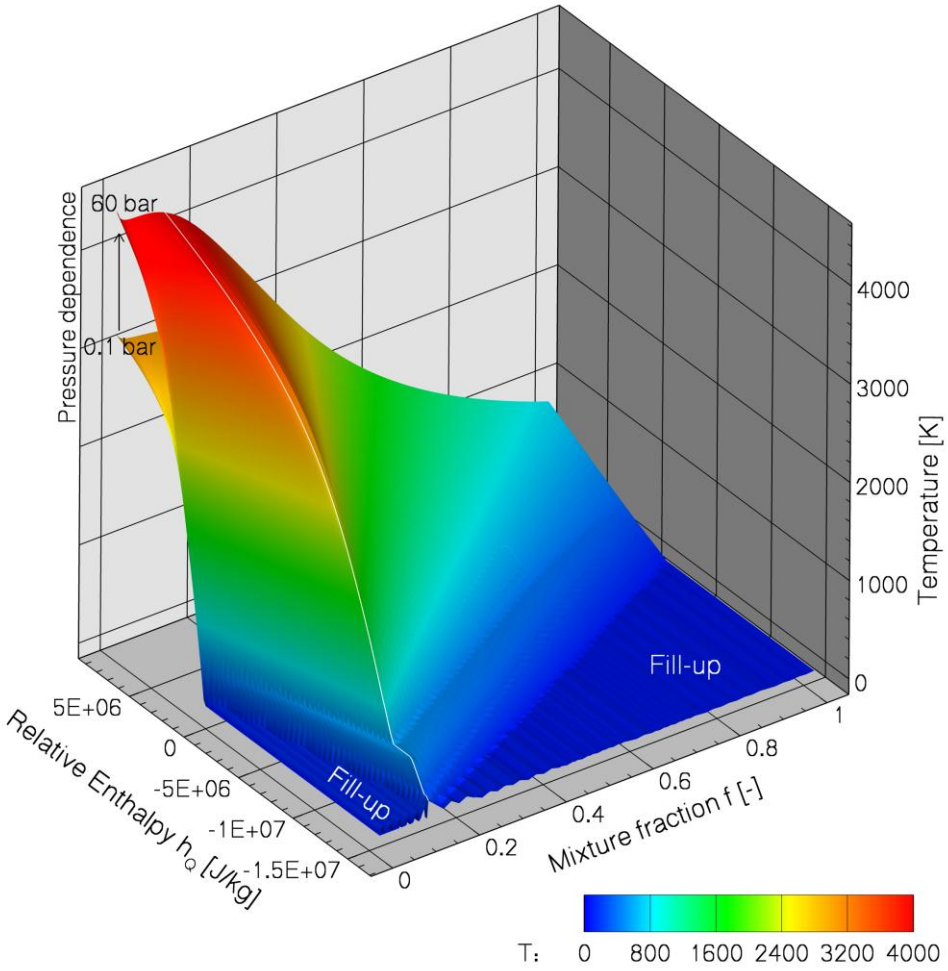

Figure 2.6: The temperature plotted over mixture fraction f and relative enthalpy h_Q for a typical H2/O2 lookup table at 60 bar. The white line marks the stoichiometric mixture fraction where the temperature has its maximum for the corresponding enthalpy level. The lower temperatures for 0.1 bar are indicated in the upper right corner.

A previous work by M. Merkle [**4**] introduced low temperature state points in the table for a Methane-LOX combustion mixture. A separate computation of the phase state of the water present in the mixture was added to the low temperature subroutine *stoffdaten.f* which made it possible for the program to adjust for condensed species in the Methane-LOX combustion mixture.

3 Changes to table generation software (CEA2FHR)

The four main issues regarding the table generation software regarded validation of the H2-LOX combustion mixture, increased of time efficiency by coupling of common blocks, lifting of the species limitation, and implementation of the compressibility coefficient. These changes are described separately below together with the effect to the table itself and the Rocflam-II simulation.

3.1 Validation

The new version of CEA2FHR updated by Merkle in [**4**] was developed and targeted for Methane-LOX combustion mixtures. Due to the short time since the completion of this program no validation of the H2-LOX combustion mixture had been made. The previous CEA2FHR version of 2010-03-09 contained much of the same structure as the new program but without the changes associated to the computation of the water phase state. The main changes in the treatment of the water phase state was that each state of water was treated separately by first determining the state before going forward with any other calculations. This made it possible to include special solutions in those phase states where problems arose. The changes are more thoroughly described in [**4**]. Another main change to the table generation program made in [**4**] was the switch to an updated non-modified version of the CEA subroutine. The former version did have customizations made by Astrium and did not include the most updated methods and constants associated with the equilibrium calculations.

The first step in validating the program for a new combustion mixture was to generate a reference table. The reference table was generated with the old version using the same input parameters as for the new. Besides the reference table the third party software REFPROP8® was also used to validate specific state points for individual species.

By comparing the output of the older program to that of the newer, differences of the properties in the various state points could be identified. If the deviations were not found to be in acceptable levels, the state point in question was analyzed further. In the following analysis the first step was to find corresponding place in the provided log file from CEA2FHR. Through implementing specific debug indicators and comparing the internal variables between the two table versions the source code could be debugged.

To discover errors dependent on certain state points the extension and resolution of the table were increased continuously throughout the validation. For larger and larger tables the method of examining individual values was abandoned and replaced with graphical representations. By plotting and comparing the dependent variables over the two more dominant independent variables, mixture fraction and enthalpy, other deviations could be found. Throughout the validation of the CEA2FHR program numerous changes and bug fixes to the source code have been made. A full account of the changes made can be seen in Appendix A.

The table generated by the final CEA2FHR version was used to compare the differences between the two tables. This was made by plotting the difference between the tables for enthalpy and mixture fraction, for a fixed pressure. The absolute or relative differences could then be evaluated over the whole table instead of individual state points.

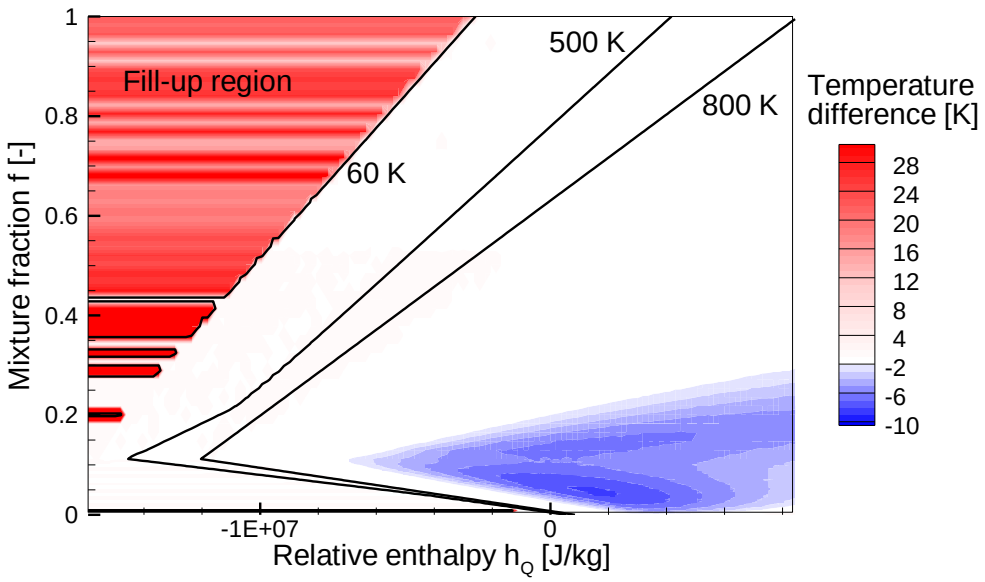

Figure 3.1: The absolute temperature difference for a typical H2/O2 table at fixed pressure (60 bar). The fill-up region difference is due to the changed minimum temperature limit between the two versions. The cooling for higher temperatures close to the stoichiometry is due to the updated version of CEA.

The absolute temperature difference plot for an H2/O2 table at 60 bar is shown in Figure 3.1. The isotherms 60, 500 and 800 Kelvin are plotted to indicate the limits for the different regions defined in Figure 2.5. The major difference is the consistent shift of 20 to 30 Kelvin in the fill-up region. This is due to the earlier version having the minimum temperature limit at 40 K instead of 60 K in the new versions. Since the last found point is filled in on the mixture fraction isoline for low enthalpies the difference propagates over the whole fill-up region. The other area of major change is the cooling

of mixture fractions around stoichiometry for higher enthalpies. This is due to the newer version of CEA being used where the constants and computational methods have been updated to the most current ones. The other variables in the table show a similar picture to the one for temperature. The absolute and relative values can differ greatly depending on the sensitivity to temperature. The heat capacity C_p for example does vary greatly between the fill-up regions of the new and older table versions.

One difference in the table identified outside the two regions mentioned above is the density. The new low temperature subroutine implemented by [**4**] takes into account the correction to the gas density due to the condensed species occupying a part of the volume. This correction is only substantial in state points of the table where practically all of the species have been condensed. Because the correction is only implemented for the lowest temperature a discontinuity between the corrected and uncorrected methods of computing the density emerges. To implement the correction for all state points with condensed species one would have to compute the specific volume of both the gas and condensed species. The density could then be corrected in the same way as described for the lowest temperature state points in [**4**].

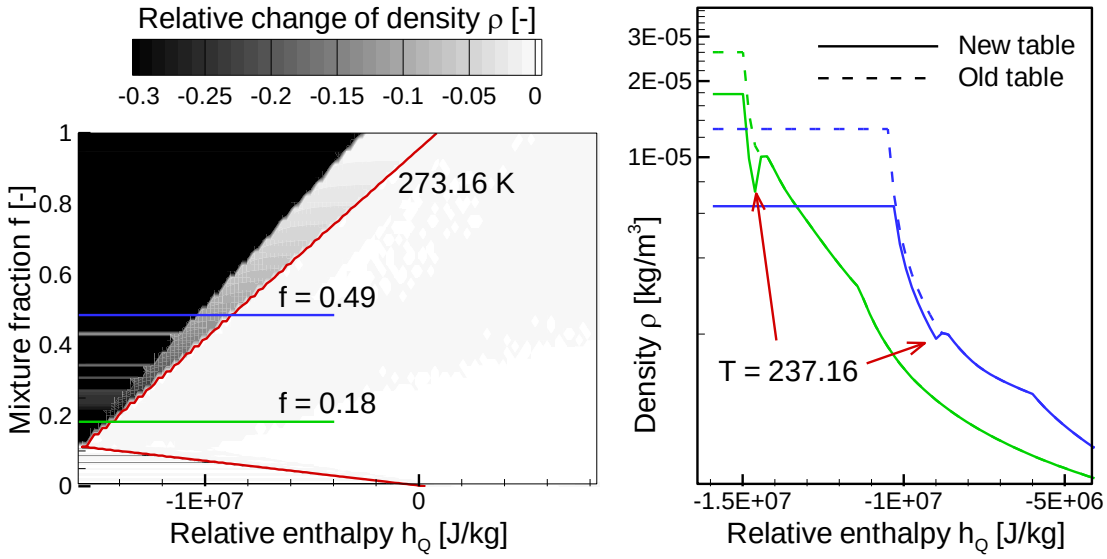

Figure 3.2: The discontinuities in density are shown to the right for two mixture fraction isolines. The isolines are again marked in the left part of the figure where the relative change of density is plotted over the whole table at fixed pressure (60bar).

Since the Rocflam-II lookup is never fully dependent on one single table state point due to the interpolation and integration this discontinuity does not propagate fully to the simulation routine. The correction is introduced when solid water is present in the mixture and discontinuity coincides therefore approximately with the 273.16 K isotherm

where the water, according to the calculations made in *stoffdaten.f,* firsts starts to solidify. The change to the density can be seen for two mixture fraction isolines in Figure 3.2. The correction effect decreases with the amount of condensed phase in the mixture which is equivalent to moving away from the stoichiometry in mixture fraction. The difference in maximum value or "roof" of the density curves is partly due to the change in temperature limit mentioned above. Another factor is that the routine does not converge exactly to the same temperature as before the change of structure of the low temperature subroutine, this because of small changes to the convergence criteria. Since the density gradients are very high in the low temperature region a change of 0.1 K can result in very large difference in the density parameter.

The viscosity and the heat conductivity are by the mixing rule dependent on the density for the low temperature region [**4**]. The change in density therefore propagates to these variables where the value can differ up to 60% in the region with solidified water. For variables in the table not dependent on either density or temperature the difference is much smaller. The heat capacity for example has a maximum deviation of 4% when not considering the fill-up region. The differences between the new and old table versions for all dependent variables are summarized in Table 3.1.

Table 3.1: Summary of difference for each dependent variable between the tables generated by the new and old generation program.

Property	**Differences between new and old table version**
Temperature	See Figure 3.1 and associated discussion above.
Total molar mass	Change mainly due to temperature change in CEA. Maximum deviation 1.1% not accounting fill-up region.
Density	See Figure 3.2 and associated discussion.
Compressibility coefficient	See Section 3.4.
Heat capacity	Maximum deviation 1% not accounting fill-up region.
Viscosity	Up to 60% due to change by the density propagated by the mixing rule. Larger differences in the fill-up region.
Heat conductivity	Up to 60% due to change by the density propagated by the mixing rule. Larger differences in the fill-up region.
Mass fractions	Changes due to temperature shift of CEA. Gaseous water differs slightly in the low temperature region due to change of structure in low temperature subroutine.

3.1.1 Simulation results

To estimate the change to the Rocflam-II simulation due to the differences between the two tables, simulations were made where the lookup table was substituted in two identical test cases. The specific wall heat flux $\dot{q}_w$ can be seen in Figure 3.3 with the solid and dashed lines representing the new respectively old lookup table. For the CALO chamber this was done for both the old and new settings with similar results. The maximum deviation of $\dot{q}_w$ is in both figures approximately 1% which is not considerably high when comparing changes of this variable in experiments (see Figure 5.7) and due to droplet distributions (see Figure 5.4).

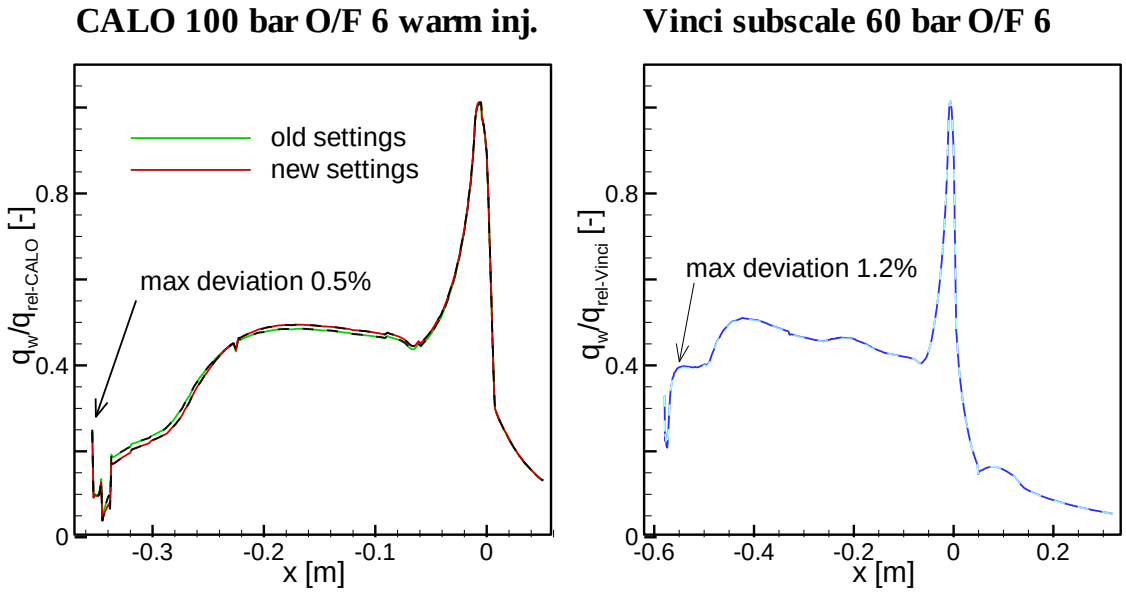

Figure 3.3: Influence of the change of table generation software on the specific wall heat flux $\dot{q}_w$ for the two test chambers CALO and Vinci subscale. The solid and dashed lines represent the new respectively old lookup table.

3.2 Common block coupling

To possibly optimize the table generation in CEA2FHR the reading of variables from the plt-file generated by CEA was moved inside the routine by reading directly from the CEA common blocks. The internal treatment between the internal CEA variables and its *OUTP* dataset is mimicked in CEA2FHR to avoid differences due to data formatting. The equilibrium properties are with this solution directly drawn from the common blocks of CEA after a *hp*-problem call to the subroutine. The CEA common blocks are therefore included into the CEA2FHR definitions (see Appendix A). With the new solution the generated table was compared to the unaltered version and no major

differences were to be found. The only consistent differences between the two tables were a somewhat different convergence for low temperature state points. In a limited number of points the extra precision of reading from the common blocks made the oxygen change phase compared to the non-coupled version.

The assumption of substantial time savings by reading directly from the common blocks was proven false by testing. In Table 3.2 the time for a set of similar simulations with different program versions are shown. The measured simulation time between the two different combustion mixtures studied does not give a conclusive result whether the common block connection speeds up the process or not. However, it is conclusive that no significant time savings are achieved by connecting the table generation program directly to the common blocks.

The inclusion of the low temperature region and GASPAK data has instead a much higher influence of the simulation time as seen in Table 3.2. The generation of the Kerosene-GOX table does not contain any calls to GASPAK data and have also no need to try to fit the equilibrium temperature to the given enthalpy as in the LH2-LOX table generation which makes the generation times considerably shorter.

Table 3.2: Table of time taken to generate a lookup table with and without common block coupling for different combustion mixtures.

Combustion mixture	**GASPAK data**	**With common block coupling**	**Without common block coupling**
LH2-LOX table	Yes	193 min	190 min
Kerosene-GOX table	No	25,6 min	26,0 min

3.2.1 Time aspect of table generation

The implemented common block connection did not cause the assumed and wanted time savings to the table generation process. One way to decrease the time spent in CEA would be to call the *THERMP* module directly from within CEA2FHR. For this to work one needs to investigate what kind of preprocessing takes place between the input file and the actual call. Noting that *THERMP* is one of the basic modules of CEA this should not be very hard to implement but it would take time to validate the functionality to be as before. One possible problem of this implementation would be that the error handling of CEA would have to be reproduced of CEA2FHR if this is not included in the *THERMP* module, something that would have to be researched. The CEA code is also to begin with written in an efficient way and any major time savings would

therefore probably be excluded. The decision of such an implementation must be held against the potential time saving. Currently the low temperature routine *stoffdaten.f* is responsible, by looking at the times in Table 3.2, for approximately 80% of the generation time required. Initiatives to time savings should according to my view be directed towards making this routine more efficient. A drastic solution would be to find packaged software capable for all of the low temperatures and thus eliminating the need to patch together many smaller limited programs.

3.3 Lifting of species limitation

Preliminary investigations showed that the main obstacle for the 12 species limitation were associated with the CEA part of the program. The investigation of CEA showed that the underlying problem was a limit of how many properties could be written in the output file for a single problem. The default limit of 20 was set by the dimension of the controlling array (*Pltvar*) associated with the input specification of the output routine [**14**]. The observed limit of 12 species was caused by a default output of 8 thermodynamically properties that also are written to the output file.

To increase the number of possible species simulated, two different solutions have been found. The first solution is built upon the common block integration of CEA in Section 3.2. By extracting the wanted thermodynamically properties directly from the common blocks instead of reading from a file the limiting output routine of CEA is bypassed. The second approach consists of changing the source code of CEA to allow more than 20 values in the output controlling array. The dimension of the array was changed to 50 and associated format entries in the code were adapted to fit the new dimension. The new value sets the effective limit to 42 species but can easily be increased if needed to in future applications. In both these ways the limitation in the output routine of CEA is eliminated and a substantial higher number of species can be imported into the table.

To test the limit lifting solution a lookup table for the Kerosene-GOX mixture were generated, which typically produces a large number of different reaction product species. The simulated mass fraction distribution for 12 respectively 13 species is shown in Figure 3.4 at injection enthalpy. The results show that of the original species only naphthalene (C10H8) changed its mass fraction distribution notably after the change from 12 to 13 species. In the 13 species generation around five percent of the naphthalene in the fuel rich region is replaced by benzene (C6H6). The mixture heat capacity (C_p) is also plotted in Figure 3.4 showing the small correction caused by the

specie change. For the different variables computed for the lookup table (see Table 2.1) it had the strongest reaction to the addition of the 13th specie.

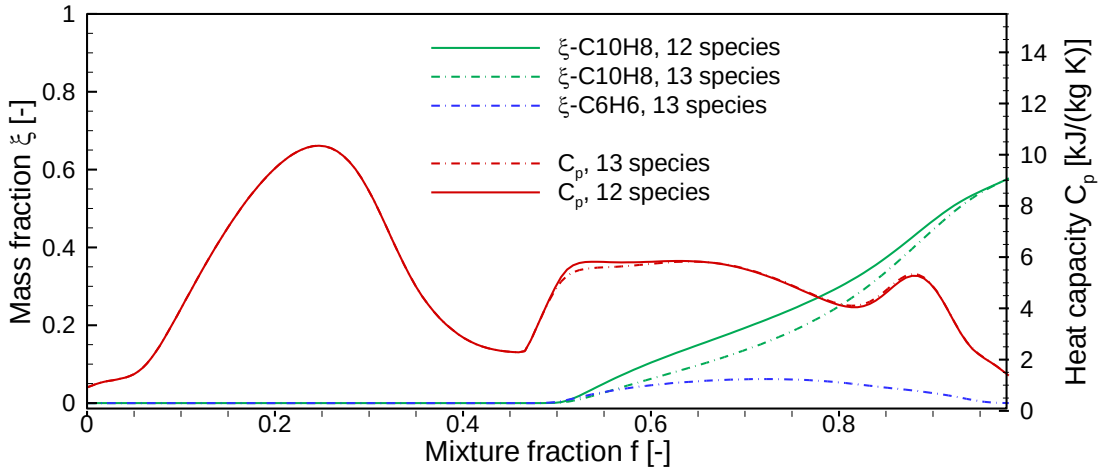

Figure 3.4: Mass fraction distribution for two table generations of Kerosene-GOX at injection enthalpy. The solid lines show the result for a simulation with 12 species versus a simulation with 13 species for the dotted lines. Naphthalene (C10H8) shows the main change by the addition of the 13th specie benzene (C6H6). Of the other properties present in the table the heat capacity had the largest influence to specie change and is also shown.

Both of the found solutions for the specie limiting problem were incorporated into the table program and can be chosen by setting of an internal boolean switch. Since the heritage error handling of CEA is associated with the reading of the output file this must always be done despite only using common blocks values. Because of this the second solution with the modified CEA source code is chosen as the default setting for the table program.

3.4 Low temperature compressibility value

The previously implemented approximation to the compressibility value in the lookup table was based on the ideal gas law (2.21). In the low temperature region where some species exist in condensed phase, and the ideal approximation of the gases no longer holds, the relation is no longer valid. To calculate a more accurate value of the compressibility the other phases must be considered by means outlined in Section 2.4. The lookup table specification from Rocflam-II defines the compressibility to be written as the inverse to the compressibility coefficient (see Table 2.1). Because of the simplifications to the mixing formulas the value of $\partial\rho/\partial p$ is firstly calculated using the formulas in Section 2.2.4. In the end of the table generation program this value is then inversed and written to the output table. The implementation of the low temperature

compressibility value is here described and the resulting effects of this to the Rocflam-II simulations studied.

Since the compressibility coefficient value only deviates greatly from its ideal approximations in the low temperature area the implementation was focused on the subroutine *stoffdaten.f* which is handling this region of the table. In every case for the water phase state in *stoffdaten.f*, GASPAK calculates the value $(\partial p/\partial \rho)_T$ for each of the gaseous species present in the mixture. With these values and mole fractions the total absolute compressibility for the gas phase can be calculated using (2.24). The calculation is here finished if no condensed species exists in the mixture. For the condensed phases of water the values of the compressibility is taken from the triple point. This solution is chosen partly to avoid computational problems where the compressibility value for the condensed phase cannot be computed. For the non-water condensed states, mainly LOX, the value is taken from the GASPAK routine. With the values provided for both the condensed and the gaseous phases the general mixing rule (2.28) is used to compute the total value for the mixture. This formula is adapted to the different water phase states in *stoffdaten.f* and only the corresponding terms for the present phases are taken into account.

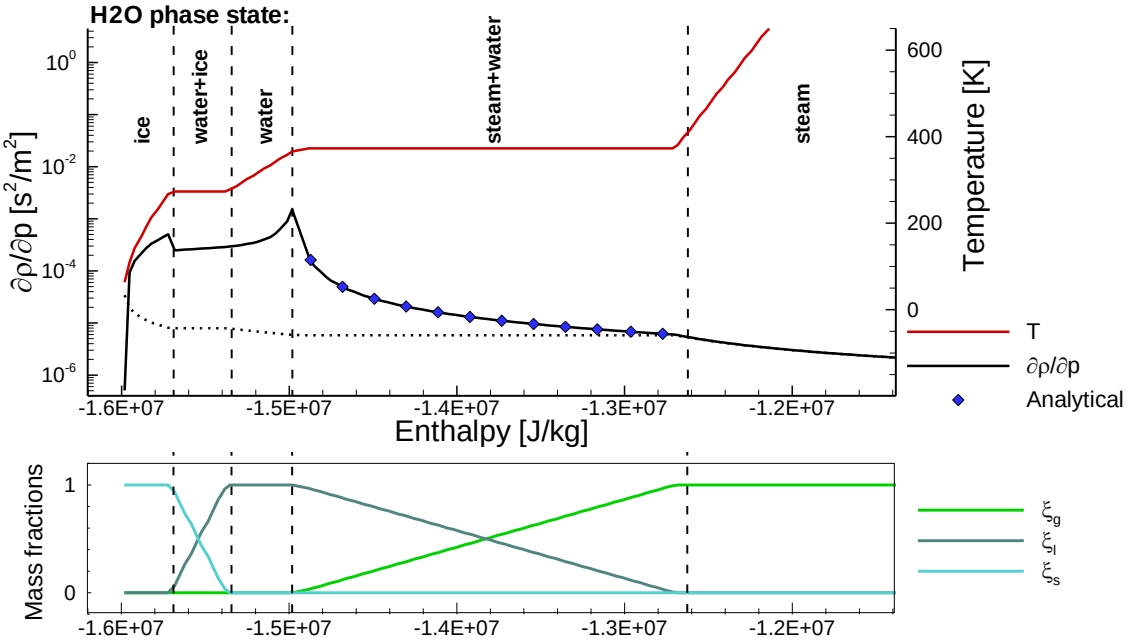

Figure 3.5: Overview of the compressibility coefficient C_ρ calculations for the low temperature region. The coefficient, temperature and the mass fractions (ξ), for each phase, are shown over enthalpy at an isoline of mixture fraction very close to the stoichiometric value $f = 0.11189$. The analytical curve (solid) shows the analytical approximation (3.1) in discrete points where it has been evaluated. The dotted line shows the ideal gas approximation of the compressibility coefficient (2.21).

To visualize the difference between the computed compressibility coefficient and the former ideal approximation the variable is plotted, for constant pressure, along a mixture fraction isoline in Figure 3.5. The relation between enthalpy and temperature can also be seen in the figure, where the temperature remains constant in the phase transition regions. The ideal gas approximation of the compressibility coefficient is here represented by the dotted line. In the figure the mixture fraction isoline calculated closest to the stoichiometry is plotted. Because of limited numerical precision in the calculation of the stoichiometric mixture fraction the isoline is displaced a tiny bit into the oxidizer rich range. This has the effect that not all of the gas in the mixture is steam. Instead is approximately 0.1‰ of the mass made out of "unburnt" oxygen.

As seen in the figure the solid curve deviates from the dotted ideal one as soon as the water in the combustion mixture starts to condense. The deviation increases with enthalpy and fraction of condensed phase to slope down again for liquid-only and liquid-solid mixtures.

The deviation in the steam and water region can be understood by looking at the mixing formula for the compressibility coefficient (2.28). First of all the solid phase parts of the mixing rule can be disregarded since ξ_s is identical to zero. In the whole water-steam region the densities of the water phases can be assumed to be constant and the liquid phase value to be two orders of magnitude greater than the gas phase value (from REFPROP8®). It can also be assumed that the mass fractions have the same order of magnitude, except in points close to the region boundary, and that the compressibility coefficient of the liquid phase is constant with temperature (2.22). These conditions makes the first term in the numerator of equation (2.28) to dominate over the entire region. The mixing rule in this region can under these assumptions be written as (3.1). This equality holds well except in the left limit of the region where very little steam is still present in the mixture ($\xi_g < 2\%$).

$$\frac{\partial \rho}{\partial p} = \frac{1}{\xi_g}\frac{\partial \rho_g}{\partial p}\left[1 + \mathcal{O}\left(\frac{\rho_g}{\rho_l}\right)\right] \tag{3.1}$$

In the calculation from the ideal gas law only the gas phase is considered and the value is calculated directly from the value for the gas form, as in (2.21). The principal difference between the two values is due to the scaling with the gas mass fraction making the mixture more compressible than in the ideal case. The higher density of the condensed phase makes the remaining gaseous phase more compressible by occupying a much smaller volume than before. The analytical formula (3.1) is evaluated in a few

points along the curve in the steam and water region and plotted with blue diamonds in Figure 3.5.

The value of the compressibility parameter in the region where ideally only liquid and solid phases should exist is dictated by the residual amount of oxygen due to inaccuracy in the calculation of the stoichiometry. The value decreases slowly because of rising density of the residual gas due to lowering of enthalpy. Over the liquid-solid phase transition it remains constant with the temperature as expected and decreases further when the temperature is once again lowered. The discontinuity in the left limit of the liquid-solid transition is due to a correction of the gas density that is only implemented in this very low temperature region (see Figure 3.2). When the residual gas finally condenses the value jumps two orders of magnitude to the value of a pure ice-LOX mixture.

A more comprehensive picture of change to the compressibility coefficient is given by looking at several isolines of mixture fraction together. In Figure 3.6 three isolines in the fuel rich region and three in the oxidizer rich region are plotted. As seen in the figure the influence of the condensing water to the compressibility coefficient increases for isolines closer to the stoichiometric mixture fraction because of the increasing fraction of H2O present in the combustion mixture.

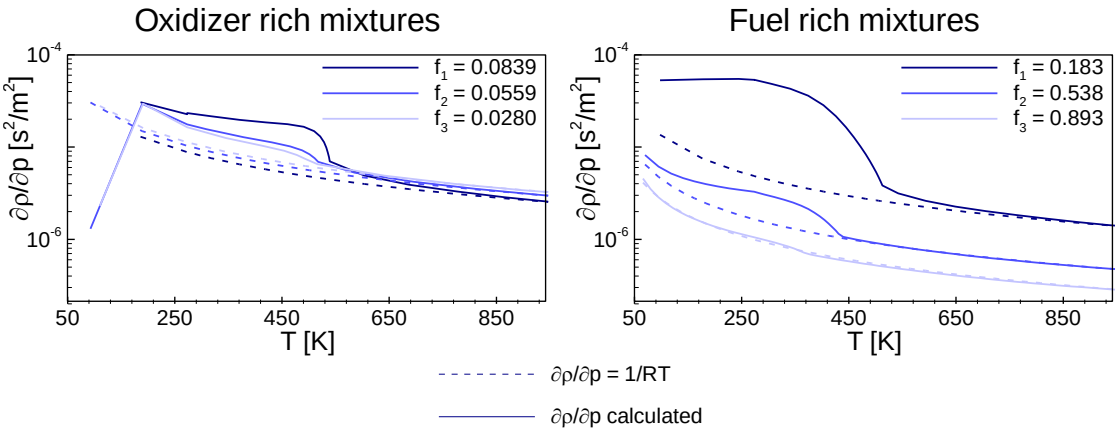

Figure 3.6: The compressibility coefficient is shown at three isolines in mixture fraction for the oxygen (left) respectively the fuel (right) rich regions. The dotted lines shows the value computed from the ideal gas law (2.21) for each of the isolines.

The different start temperatures for the condensation for the different isolines are due to the differing partial pressures of the steam. In the oxidizer rich mixtures the curves end by a steep drop to a significantly lower value. This is the same behavior as described for the almost stoichiometric mixture where the residual oxygen condenses and the mixture becomes a pure liquid-solid mixture (see Figure 3.5). In the fuel rich mixtures, where

the residual gas (H2) has a much lower condensing point which is not reached by the lowest enthalpy in the table, this does not happen. Instead the curve tends back towards the ideal curve when all of the steam has condensed in the mixture. This is clearly shown for the fuel rich f_2 curve where the gradient for the lower temperatures coincide for the ideal and calculated curves.

3.4.1 Simulation results

The influence of the compressibility to the Rocflam-II simulations is described in Section 2.2.4. To investigate the effect of the changed compressibility coefficient on the convergence behavior the simulation parameters of a cell node in the middle of the chamber were studied. A simulation of the Vinci subscale chamber, with the altered lookup table, was performed with 95 000 solver steps and 15 injection events. In Figure 3.7 the behavior of five simulation parameters (pressure excluded because of very small gradients) in a monitor point are shown over the course of the simulation. After 80 000 steps the Lagrange module is turned off and the simulation is left to converge in "frozen" mode, with the sources created by the droplets in fixed position.

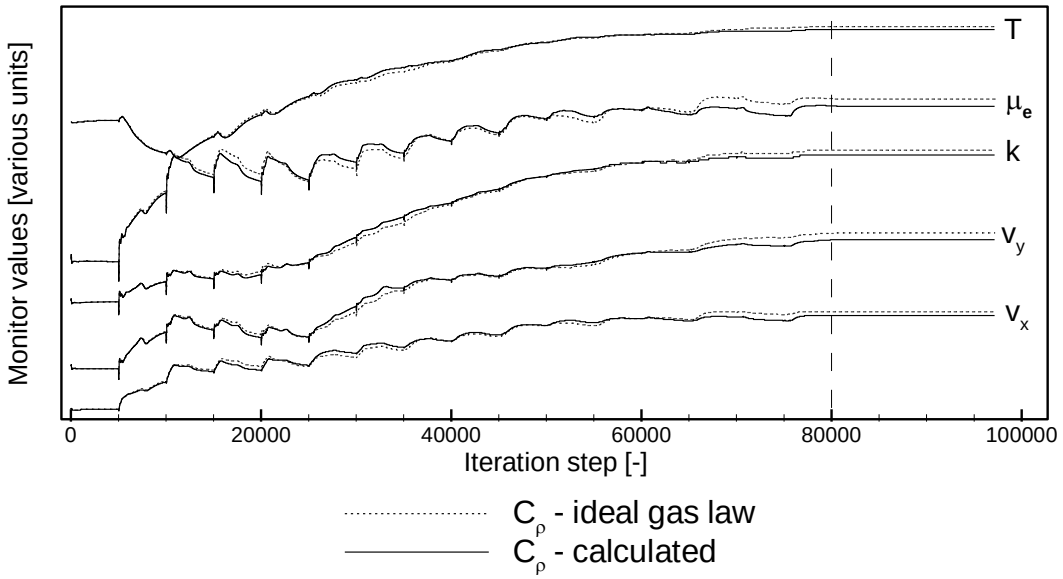

Figure 3.7: Figure showing the convergence behavior for two simulations where the compressibility coefficient differs between them. The five most varying simulation parameters for a node in the middle of the combustion chamber are shown over 95 000 solver iterations. Every 5 000th step, until the dashed line at 80 000, an injection event is triggered. The simulation parameters are (listed from above): Temperature, effective viscosity, turbulent kinetic energy, radial (y) and lengthwise (x) velocity.

As seen in the figure the coefficient changes have a very small influence of the behavior compared with the changes caused by the injection events. The resulting deviation is below 1% for all steps and parameters in this monitor point. The change does also have a very small impact on the final performance values of the combustion chamber. The maximum change in final performance values is below 0.03‰. The convergence behavior overall cannot be said to worsen or improve in a significant way since the different curves have the same overall shape. The main conclusion drawn is that the change to the compressibility coefficient in the low temperature areas does not have a significant impact on neither the convergence nor the simulation results.

The correction to the low temperature compressibility of the table was not included in the simulation lookup tables in Chapter 5. This was mainly due to time constraints since the simulations were initiated before the final validated CEA2FHR version, with the low temperature compressibility, was done. A qualified guess for the results of the CALO and Vulcain 2 thrust chambers, looking at the results for the Vinci subscale chamber above and keeping in mind the role of C_ρ in Rocflam-II simulations, would be that the changes to the final performance values are negligible.

4 Lookup table resolution study

Through former investigations of the table resolution [**5**] there exists values for the higher limit of the resolution where no difference can be seen in the simulation. With the newly developed structure of CEA2FHR the generation time is significantly longer and the in [**5**] suggested resolution would yield generation times in the order of days with the new structure. There also exists praxis at Astrium with default values for the resolution that are significantly lower than the suggested higher limit. The default values instead generate lookup tables on the order of hours. To form a more complete picture of the dependency between the table resolution and the simulation a study is performed below where each of the resolution parameters for the table is studied individually.

4.1 Test case: Vinci subscale

To test the influence of the lookup table resolution to the simulations the Vinci subscale H2/O2 rocket combustion chamber was chosen as test case. The Vinci subscale chamber is a smaller version of the full-scale Vinci combustion chamber developed for the upper stage of Ariane 5. The subscale chamber does only contain 2 sets of injection element rows, plus a single one in the center, compared with 6 rows in full-scale. It is also about 2.5 times smaller in diameter to its bigger twin. The subscale model is used in simulation for those cases where the extra amount of computer power and time can be spared instead of doing a full-scale simulation. The load point for the subscale chamber is chosen to mimic the full-scale conditions and was kept constant through all variations of the lookup table. The main parameters for the load point are shown in Table 4.1.

Table 4.1: Parameters for the Vinci subscale load point used for lookup table resolution study.

Load point	p_c	O/F	$\dot{m}_{H2}$	$\dot{m}_{O2}$	$T_{H2,inj.}$	$T_{O2,inj.}$
R1	60 bar	6	0.75 kg/s	4.5 kg/s	~200 K	~100 K

In Figure 4.1 a typical contour plot of the temperature is shown for the Vinci subscale chamber. The two injection rows together with the central injection element can be identified by the five flames visible in the chamber.

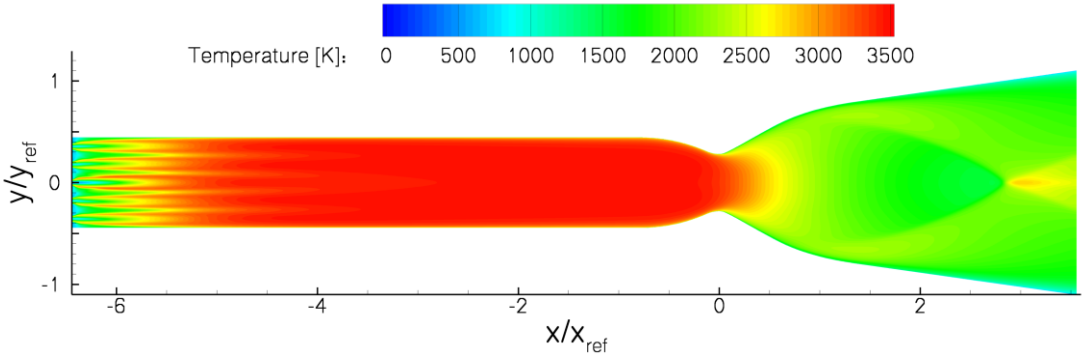

Figure 4.1: A typical contour temperature plot for the Vinci subscale combustion chamber at the R1 load point specified in Table 4.1.

The mesh of the chamber is made up out of 558x133 cells with a higher resolution in the area close to the wall, this to be able to better describe the interaction of the gas with the wall. Since no film cooling is applied in the chamber this module is turned off in Rocflam-II and possible condensation of water to the wall is handled by a higher density in the gas phase.

To study the influence of the lookup table resolution as much as possible of the simulation was kept constant, including the starting conditions. The direct dependency of the converged solutions to the lookup table could be studied by interchanging the tables and interpreting the final simulation results. The resolution of the table is controlled for each of the three dimensions; pressure, enthalpy, and mixture fraction. The resolution of the mixture fraction is divided into one oxidizer rich and one fuel rich side which can be controlled independently. Because of this the fuel- and oxidizer rich settings are treated as different dimensions.

Each of the main dimensions of the table was studied individually by generating tables with differing resolution. The active dimension was varied around the default value given by the former settings while the others were kept at their default values. After generating a table with the chosen resolution a simulation was started and let to run until the residuals indicated convergence. To be able to stronger guarantee convergence for the different simulations, an initial simulation run setting of 90 000 solver steps with 17 injection events were chosen. After this run the simulation was restarted without the Lagrange module and left to converge. This occurred in most cases within 15 000 solver steps. A typical evolution of the residuals in such a simulation is shown in Figure 4.2. Due to influence of a stochastic force in the Lagrange module the residuals increase sharply at every injection.

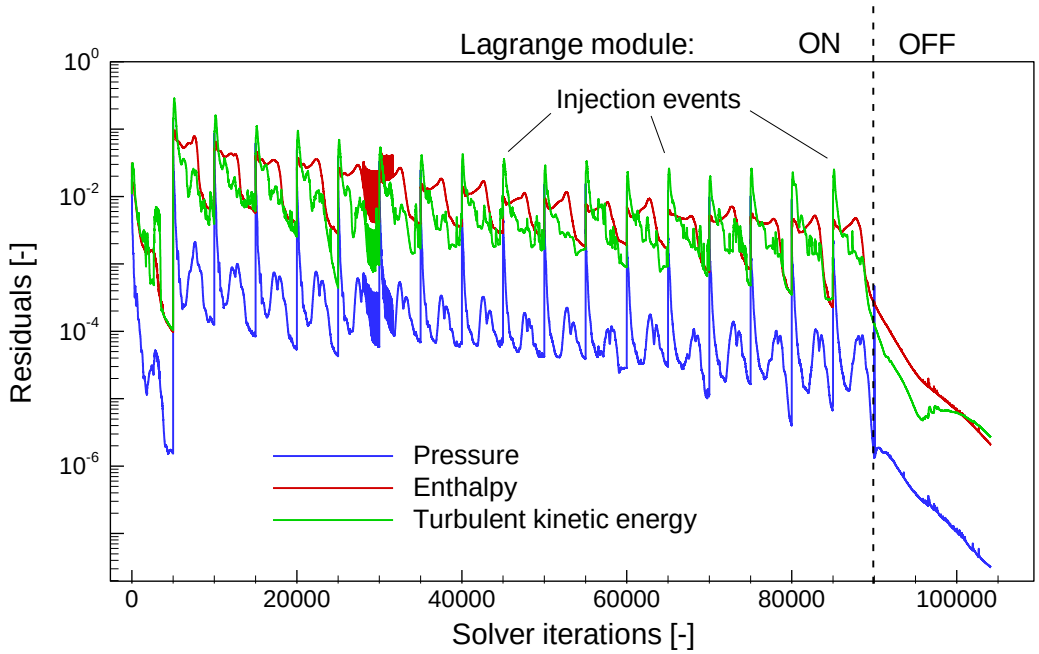

Figure 4.2: The residuals for pressure, enthalpy and the turbulent kinetic energy for a typical simulation to investigate the table resolution. After 90 000 solver steps and 17 injection events the Lagrange module is turned off and the solution converges quickly.

The different properties of the individual table dimensions made it unsuited to vary all of them uniformly around the default value. Instead the resolution for each dimension was lowered to a limit where substantial change to the simulation could be seen, alternatively the simulation routine was not accepting the altered table because of its sparseness. In the higher limit the resolution was increased up to 150% of the default setting.

To find a quantitative way of estimating the precision of the simulation, four different indicators were chosen. The characteristic velocity c^* and the specific impulse I_{sp} were chosen from the common performance parameters of a rocket engine (see Section 2.1). Since both of these variables are crucial in investigating a design choice it is important that they are as accurate as possible. The third indicator was chosen to be the temperature average of the whole combustion chamber. Because of the direct dependence to the lookup and interpolation from the table of temperature this provides a good view into the precision of this process. As a fourth indicator the stagnation pressure in the throat was chosen as a performance indicator.

The final validated version of the low compressibility value was due to time constraints not included in the table resolution study. The main argument for this was that a change in the lookup table, although showed to have a small influence on the simulation results

(see Section 3.4.1), would corrupt the changes of simulation precision observable in the study by introducing an extra parameter. The alternative would be to have redone all simulations up to the point where the final CEA2FHR version existed which would be hard to have managed time wise.

4.2 Resolution dependency

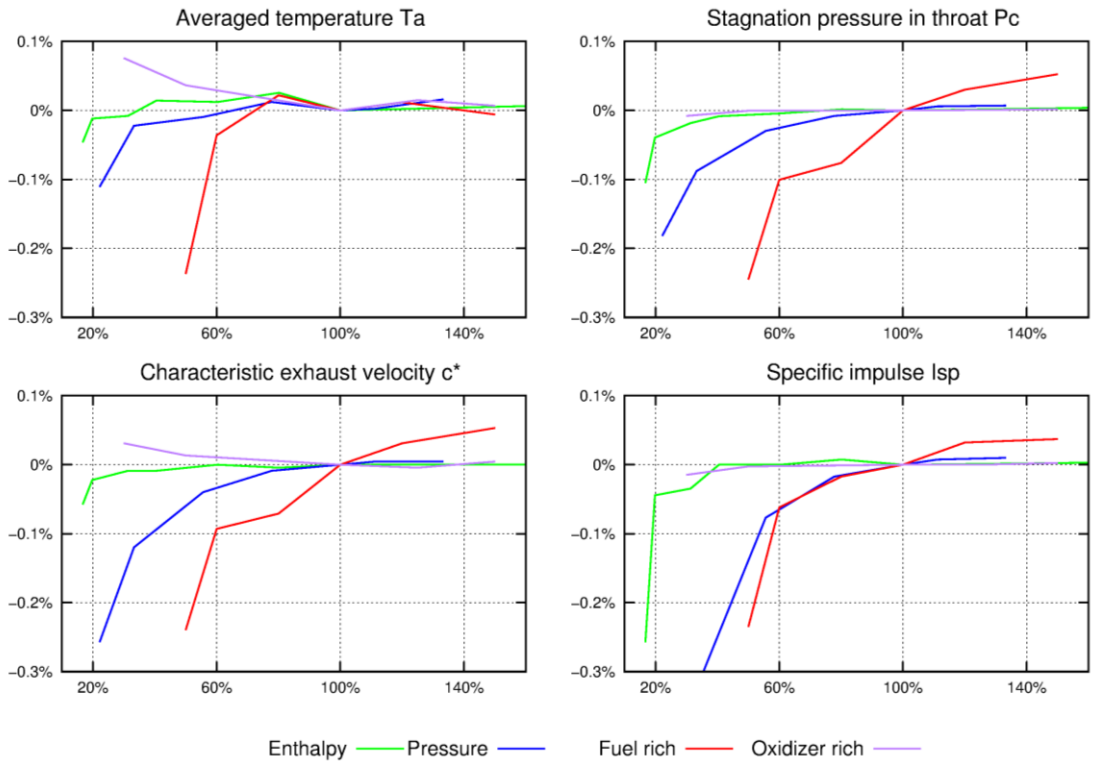

Figure 4.3: Figure showing the dependencies of four simulation indicators to the resolution of the four lookup table dimensions: Enthalpy h_Q, Pressure p, Mixture fraction f of the fuel rich respectively oxidizer rich side. The x- and y-axis represent the resolution respectively the deviation of the specified indicator.

Four indicators of the simulation result are plotted with respect to the table resolution in Figure 4.3. The deviation against the normal value of the current resolution is plotted against the relative resolution change for the different dimensions of the table.

When looking closer at the simulations performed for the enthalpy it could be seen that the major influence of the lower enthalpy resolution was the way the condensed species were treated. The amount of condensed species indicated of the inner wall of the chamber for the lowest resolved table deviated greatly against the normal case. With lower enthalpy resolution the distinction of the phase regions in the low temperature

ranges of the table becomes smaller and thus is the precision of the simulation decreased for this region. This can be seen in the upper left of Figure 4.4 where the resolution at 16% of the default value completely fails to resolve the transition from liquid to solid phase.

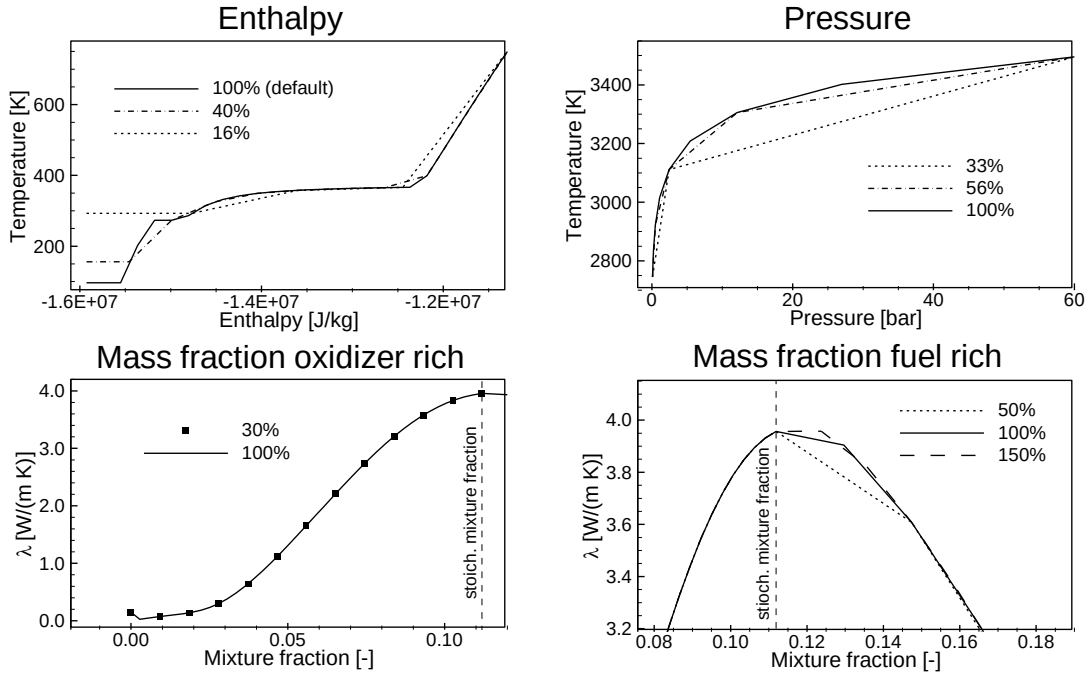

Figure 4.4: Figure showing the main influence of the dimensions to the lookup table. The figures are showing (listed from top left): Effect of enthalpy resolution for the low temperature region, effect of pressure resolution for the temperature at stoichiometric mixture and injection enthalpy and the heat conductivity (λ) over mixture fraction at injection enthalpy.

The table resolution of the pressure dimension has a significantly greater influence of the performance precision than the enthalpy as seen in Figure 4.3. The greatest deviations in the simulations for the pressure dimension are found in the nozzle where the pressure is far from the chamber pressure. With lower resolution and the same limits for the pressure in the table the precision of the variables becomes worse because of the exponential relation to the pressure. In upper right of Figure 4.4 the large deviation for lower pressures can be seen as the resolution is lowered.

Absolute resolution of the fuel rich and oxidizer rich ranges differ greatly for the default setting of the table. The oxidizer rich range has in the default settings a relative resolution of 0.28% of the total mass fraction range between each point. This is about six times higher than the value for the fuel rich range that has a relative resolution of 1.78%. The resolution investigation in Figure 4.3 shows this relation clearly in the fuel rich range being significantly more sensible to changes of resolution than the oxidizer rich range. One reason for this kind of unbalanced default setting is that the gradients of

the oxidizer rich region are much higher than those in the fuel rich region. This is especially true for the density (ρ) and transport properties (μ, λ) since the values between unburnt cryogenic oxidizer at $f = 0$ and gaseous water at stoichiometry differs greatly. In the lower part of Figure 4.4 the gradient for the heat conductivity λ is shown for both the fuel and oxidizer rich side.

4.3 Recommendations regarding choosing table resolution

From the simulations regarding enthalpy resolution shown in Figure 4.3 a weak coupling between resolution and precision for the performance parameter can be seen. This gives the indication that a decrease in enthalpy resolution could be possible without losing precision of the simulation. In the low temperature region where condensed and solid species are present the temperature changes very rapidly. Since no adaptive distributions of the enthalpy levels are in place where the low temperature region could be sampled denser than the rest of the table the current resolution is kept as the default one at 40% of the injection enthalpy between each level. This is the simplest way to retain consistency and accuracy for the condensed species values.

The current pressure level distribution is made in an exponential way between the highest and lowest entered pressure point. This distribution covers the gradients in an efficient way and since Figure 4.3 shows that no substantial precision can be gained in increasing this number the resolution is kept at its default level for the pressure dimension.

The fuel rich mass fraction resolution shows in Figure 4.3 potential to increase precision of the indicators by increasing the resolution. This is shown by it not having the same convergence against the nominal values as shown by the other three table dimensions. For three of the indicators a potential increase of precision around 0.5‰ is shown. The relative low increase in precision makes the increase a consideration between the precision and increased time for generating the table.

A part of the loss of precision for the fuel rich side can be traced back to large gradients which is not fully resolved in the fuel rich region. This can be seen in lower right of Figure 4.4 where the nominal resolution does not fully resolve the maximum of the heat conductivity λ close to the stoichiometric point. Another cause to the loss of precision for this case is a uniform change of the temperature throughout the chamber. This could

in turn be traced back to a somewhat different interpolation of the temperature with a sparser mesh in the fuel rich region of the table.

The overly resolved oxidizer rich side has a negligible influence to the performance of the simulation as shown in Figure 4.3. Closer studies of the lookup table also show that there exists an opportunity to lower the resolution but still resolving the large gradients on this side. The lower left of Figure 4.4 shows that approximately one third of the current resolution would be enough to resolve the heat conductivity gradient fully.

All into account for the mass fraction resolution the suggested change is to decrease the resolution of the oxidizer rich region while increasing it for the fuel rich region. The new settings would enable to possibly raise precision with 0.5‰ while not influencing the time taken to generate the lookup table.

Since the scope of this resolution investigation does only contain the Vinci subscale combustion chamber it is hard to extrapolate for what settings should be recommended for other types of engines and fuel combinations. For other fuel mixtures such as Kerosene-GOX it is possible that the relationship between the resolution and the performance precision looks somewhat different because of different size and placement of property gradients.

5 Simulation of combustion chambers

In the past there has been a difference in the treatment between the cryogenic H2/O2 propellants and the other combinations such as MMH-NTO (MonoMethylHydrazine - Nitrogen Tetra Oxide) and Methane-LOX in Rocflam-II simulations. To consolidate the Rocflam-II simulation software further and increase consistency and transparency of the source code, work has been made to remove some of these differences. The changes to the source code and their effect on the simulation results are described in Section 5.2. For the new formulation correction functions for the droplet distribution are computed (see Section 5.3) using simulation of the CALO test setup (see Section 5.1). Finally the results of the new settings are shown for the CALO (see Sections 5.4 and 5.5) and Vulcain 2 (see Section 5.6) combustion chambers and compared to results of the previous Rocflam-II settings.

5.1 CALO combustion chamber

The CALO (Calorimetric) test setup is a subscale H2/O2 combustion chamber with the option of measuring the heat flux through the wall in separate segments using annular calorimeters distributed along the symmetry axis of the chamber. For each of the wall segments the resulting heat flux of the combustion can be measured by the coolant enthalpy increase. The main purpose of the test chamber is to analyze the heat flux to determine the need for cooling of the designed chambers and evaluate the combustion efficiency and performance of different injection elements. The whole system can be simulated by coupling Rocflam-II, for the combustion in the chamber, to RCFS-II, for the coolant flow around the chamber. A measure of the accuracy of the simulation can be made by comparing the heat flux computed from the simulation to the experimental data attained from the CALO experiments.

The spray combustion method is similarly implemented for the CALO chamber as for the previously mentioned Vinci subscale chamber (see Section 4.1). The hydrogen fuel is injected directly into the gas phase as source terms. The oxidizer LOX is injected in droplets and these are tracked throughout the chamber by the Lagrange module. Typical contour plots of the temperature and O/F for the CALO test chamber are shown in Figure 5.1.

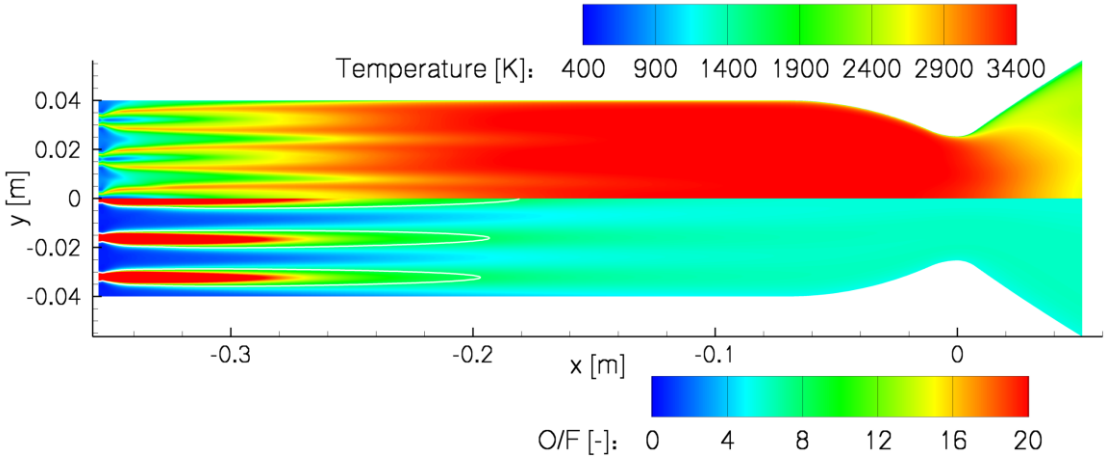

Figure 5.1: Contour plot for the temperature (top) and O/F (bottom) for the CALO test chamber in the 70-6 load point (warm injection). The white lines in the lower plot indicate stoichiometry ($O/F = 7.937$)

Two modes of injection are used in tests of the CALO chamber. One where the fuel is injected at cryogenic temperature at approximately 90K called the "cold" mode. The other one is the "warm" mode where the fuel is preheated to a temperature around 200K. For each of these modes there exists a set of tests that have been performed at different chamber pressures and O/F ratios. A compilation of the load points for both injection modes can be seen in Figure 5.2.

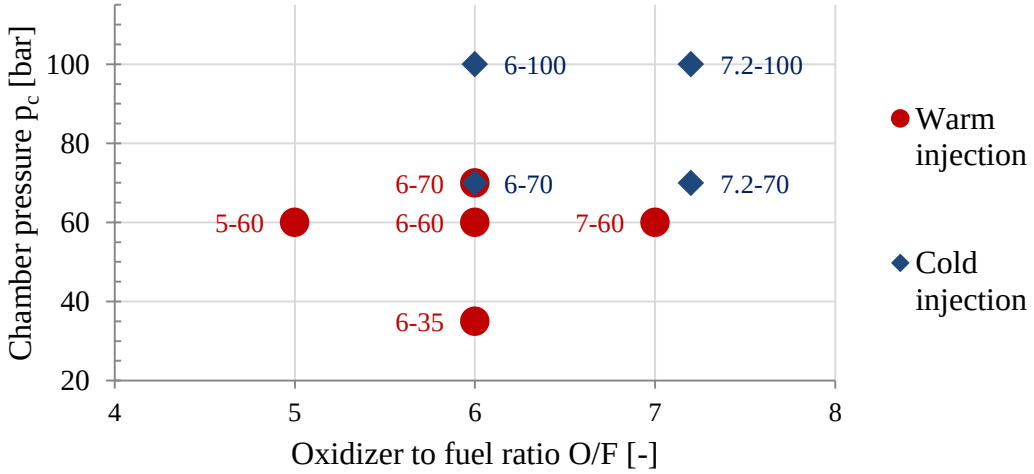

Figure 5.2: Compilation of load points for the cold and warm injection of the CALO combustion chamber.

The CALO chamber mesh is made out of 323x133 cells and has as the Vinci subscale mesh a higher resolution in the area close to the wall and in the throat region. Because of the significance of the CALO chamber in comparing the simulation to experimental data it is a good candidate to further validate the new table generation software. The

computed wall heat flux results are similar to the ones observed for the Vinci subscale chamber validation (see Figure 3.3 and Section 3.1.1).

5.2 Rocflam-II formulation change

The changes associated with the Rocflam-II source code are mainly concerned with the simulation of the droplets. The first of these changes is the value of the binary diffusion coefficient C_{diff} controlling the reaction between the droplet "atmosphere" and the gas phase (see Section 2.2.1). The influence of the C_{diff} value on the oxidizer vaporization in the CALO chamber is shown in Figure 5.3. Through investigations in [**6**] a new value for this Rocflam-II input setting has been recommended. The change is associated with the fact that earlier sources have been using an approximation of the atmosphere surrounding the droplet. This approximation consists of the droplet atmosphere having the properties of gaseous H2O instead of the droplet specie. In the new version of the source the "true" atmosphere properties are included into the binary diffusion reaction of the atmosphere diffusing into the gas phase. The new C_{diff} value is for this situation calculated with the O2 atmosphere diffusing into the surrounding gas phase approximated by pure H2 gas. Since the reaction is binary this also holds for the reverse reaction if condensed H2 droplets were to be injected. The approximation of pure H2 gas instead of the surrounding gas phase mixture has been investigated in [**6**] and the change to C_{diff} found to be negligible.

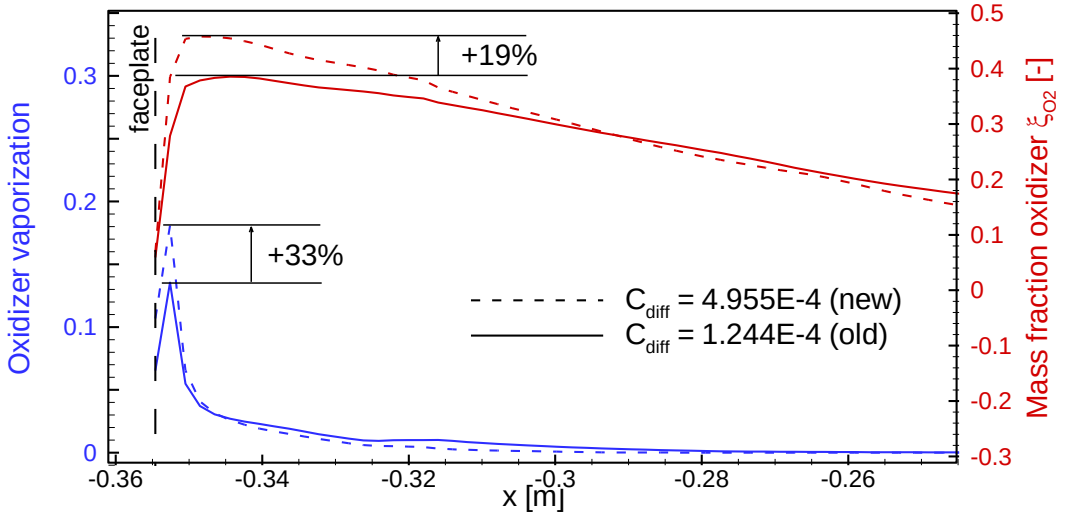

Figure 5.3: Figure showing the influence due to change of C_{diff} to the vaporization and presence of oxidizer along the combustion chamber. The radially integrated values are here shown in the direct vicinity of the faceplate at $x = -0.355\ m$ for the CALO chamber.

The second change is an inclusion of lower temperature properties to the data blocks that the main program reads from. This is necessary for the source to have thermodynamically properties of the "new" atmosphere of the droplet for all atmosphere temperatures.

5.3 Droplet distribution correction

One of the primary influences on the sources from injected condensed phase droplets is the MMD. A change in distribution of the injected droplets means differing evaporation rates along the trajectories simulated by the Lagrange module and thus placement and size of the sources in the gas phase. Since smaller droplets are vaporized at a higher rate than bigger ones, the total distribution of oxidizer sources is displaced further into the chamber with increasing MMD. Figure 5.4 shows this behavior in simulation for the 70-6 load point of the CALO test chamber with warm injection. The increase in mixture ratio in the front part of the chamber translates to a higher wall heat flux in this region due to increased combustion.

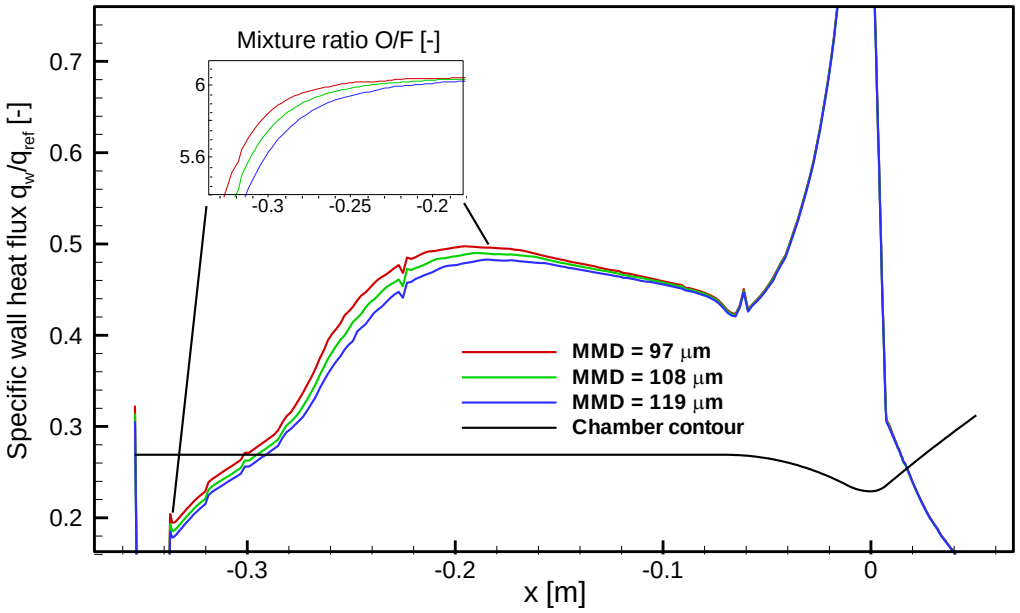

Figure 5.4: Figure showing the specific wall heat flux of the CALO chamber at 70 bar, $O/F = 6$ and warm injection. The distribution of the mixture ratio O/F and the wall heat flux $\dot{q}_w$ are shown for three different oxidizer droplet distributions with varying MMDs.

Because of the large influence to the predicted wall heat flux the MMD parameter has undergone a great deal of scrutiny from Astrium. In [**5**] and [**8**] a possible droplet

distribution theory suggested from literature is studied. With increasing σ the width of the distribution increases, as seen in Figure 2.3, making for a larger part of smaller droplets in the spray. To test the influence of σ to the wall heat flux a set of simulations were performed were the expectancy value was kept constant while varying σ. The results in Figure 5.5 show that the increases in width and displacement of the droplet distribution have a similar influence on the specific wall heat flux as the MMD, in line with the results of a similar investigation in [**17**]. To limit the number of controllable variables for finding an acceptable droplet distribution the shape parameter is fixed at 0.2.

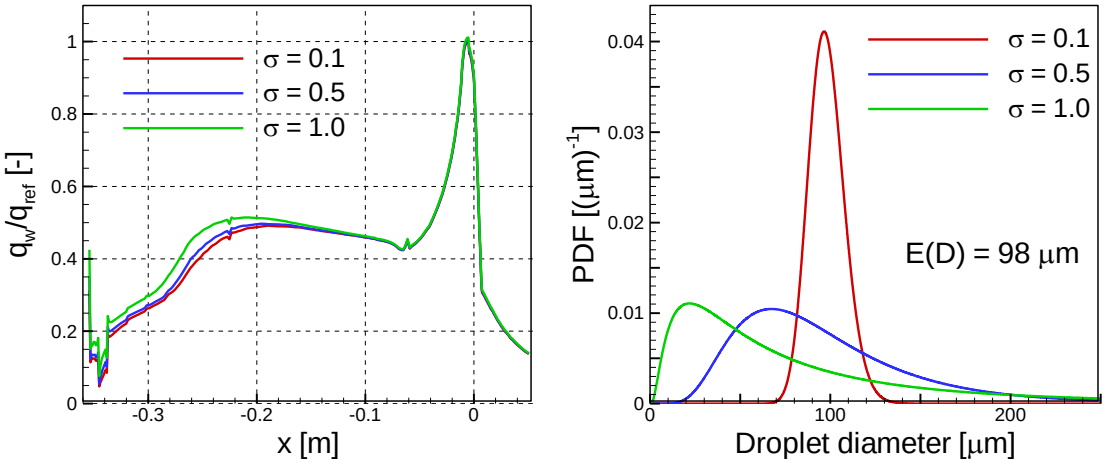

Figure 5.5: Influence of the droplet distribution shape parameter σ to the specific wall heat flux and the droplet simulation for a typical CALO simulation.

The current method at Astrium of estimating the MMD of the droplet distribution for H2/O2 coaxial elements is based on the results of Vingert et al. [**11**]. Vingert proposes two different empirical formulas (see Section 2.2.2) of determining the SMD of a droplet atomization caused in the shear layer between two fluid jets. The two formulas produce a similar value and as a standard approach is the average taken as the first estimation of the droplet distribution inside the chamber. The estimated SMDs for the injection conditions of the CALO load points for the two different methods, together with the corresponding MMDs, for a distribution with $\sigma = 0.2$, can be seen in Table 5.1.

Table 5.1: Results from empirical formulas for the injection conditions of the CALO load points. The MMD is found by taking an average of the empirical SMD (see Section 2.2.2) and adding a log-normal form factor (2.11).

Load point	**SMD** (2.10) [μm]	**SMD** (2.9) [μm]	**MMD** [μm]
70-6	91.2	91.1	93.0
70-7.2	96.9	96.9	98.8
100-6	86.9	86.6	88.5
100-7.2	93.0	92.9	94.9
35-6	49.0	47.5	49.2
60-5	45.9	44.3	46.0
60-6	49.3	47.8	49.6
60-7	54.0	52.5	54.3
70-6	51.2	49.6	51.4

The MMD values presented by the literature differ from the MMD values that the Rocflam-II simulation predicts should be simulated to achieve the experimentally measured specific wall heat flux. To try to estimate the difference between the experiments performed in [**11**] with water and helium to the experimental situation of H2/LOX under combustion a correction factor y is introduced and defined in (5.1).

$$y = \mathrm{MMD}_{\mathrm{simulation}}/\mathrm{MMD}_{\mathrm{literature}} \tag{5.1}$$

The correction factor between the literature and simulation adaptions to the experimental data suggests an exponential or linear dependency to the mixture ratio O/F. Exponential and linear fits return similar values in terms of fit to data but because of the very limited amount of data no conclusion can be drawn. The correction factor is finally chosen to be on exponential form to be able to approximate values also in low O/F ratios. The linear approach would return a negative value on the MMD which would be unusable for other low O/F configurations such as gas generators. The correction factors for cold and warm injection together with their corresponding exponential correction functions can be seen in Figure 5.6.

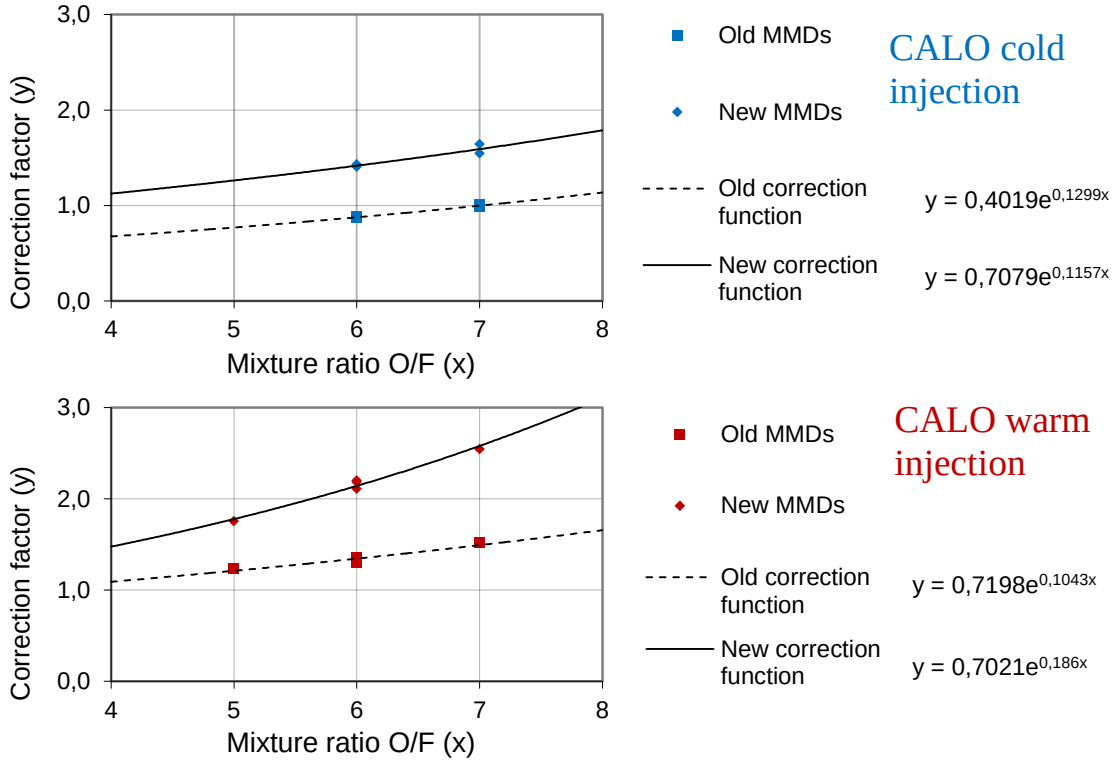

Figure 5.6: Correction factors between the literature and values suggested for the experiment by Rocflam-II for the droplet distribution plotted over the global mixture ratio O/F for the cold and warm injection modes. An exponential correction function is fitted to each data set to determine the function to be used for other mixture ratios.

5.4 CALO cold injection simulations

For each of the cold injection load points a corresponding Rocflam-II simulation was performed where the new values of the C_{diff} parameter and corresponding change of the Rocflam-II formulation were taken into account. The simulation was allowed to couple 30 times with the RCFS-II module and after convergence the gas phase was allowed to converge separately. Between each of the RCFS-II couplings the Navier-Stokes solver performed 3 000 steps with two injection events at iterations 1 000 and 2 000. The MMD value was swept over a range of values to best fit the experimental data for the wall heat flux. In Figure 5.7 the heat fluxes for the final settings are shown for each of the load points together with the old settings and experimental data.

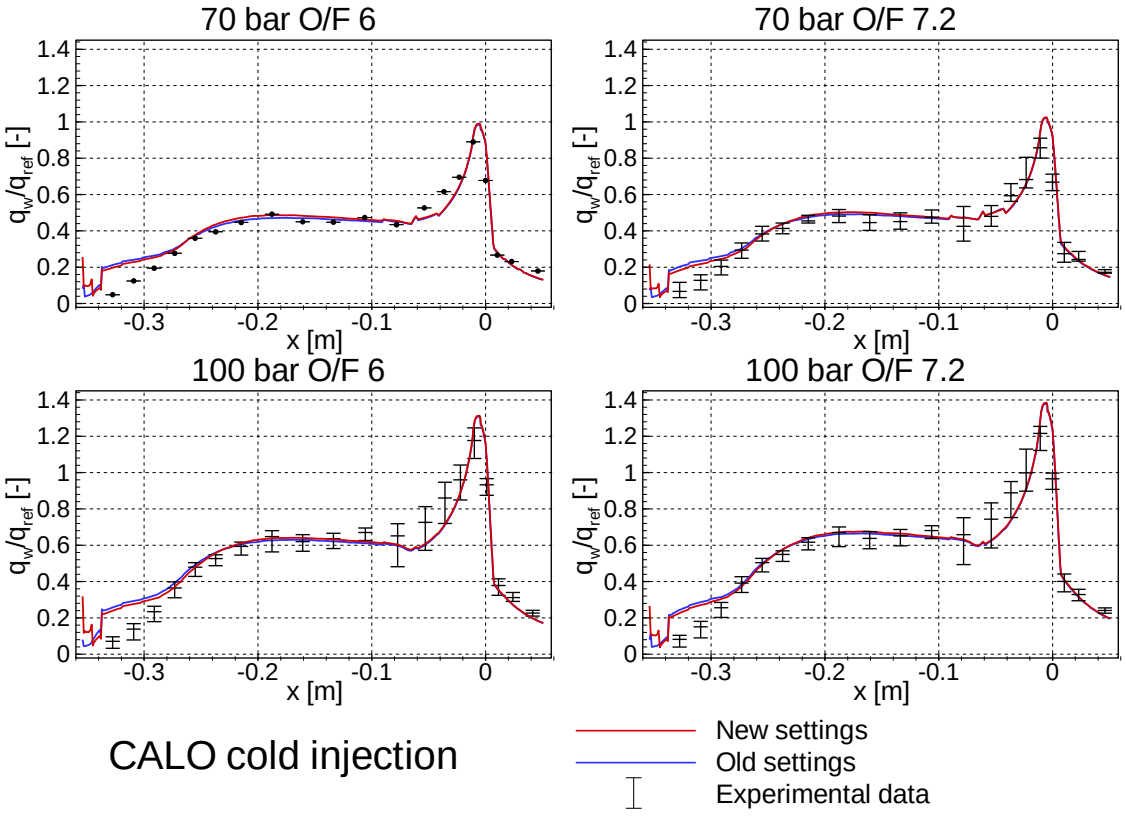

Figure 5.7: The wall heat flux $\dot{q}_w$ for the four cold injection CALO chamber load points. The new final settings are shown together with the old settings and experimental data.

As seen in Figure 5.7 the new settings almost entirely match the previous settings for the cold injection mode of the CALO chamber. The greatest deviation can be seen close to the faceplate in the very front of the chamber. This change is due to a Rocflam-II formulation change not taken up by this report that has taken place in the time between the two setting adaptations. One small trend visible is that the newer setting has a somewhat better fit to the experimental data in the first third of the chamber.

5.5 CALO warm injection simulations

An analog method to the one used above was used to find the new MMD settings for the warm injection CALO chamber load points. Rocflam-II was coupled 30 times to the RCFS-II module with 4 000 solver steps between each coupling. The injection event was triggered one time at step 2 000 of each cycle.

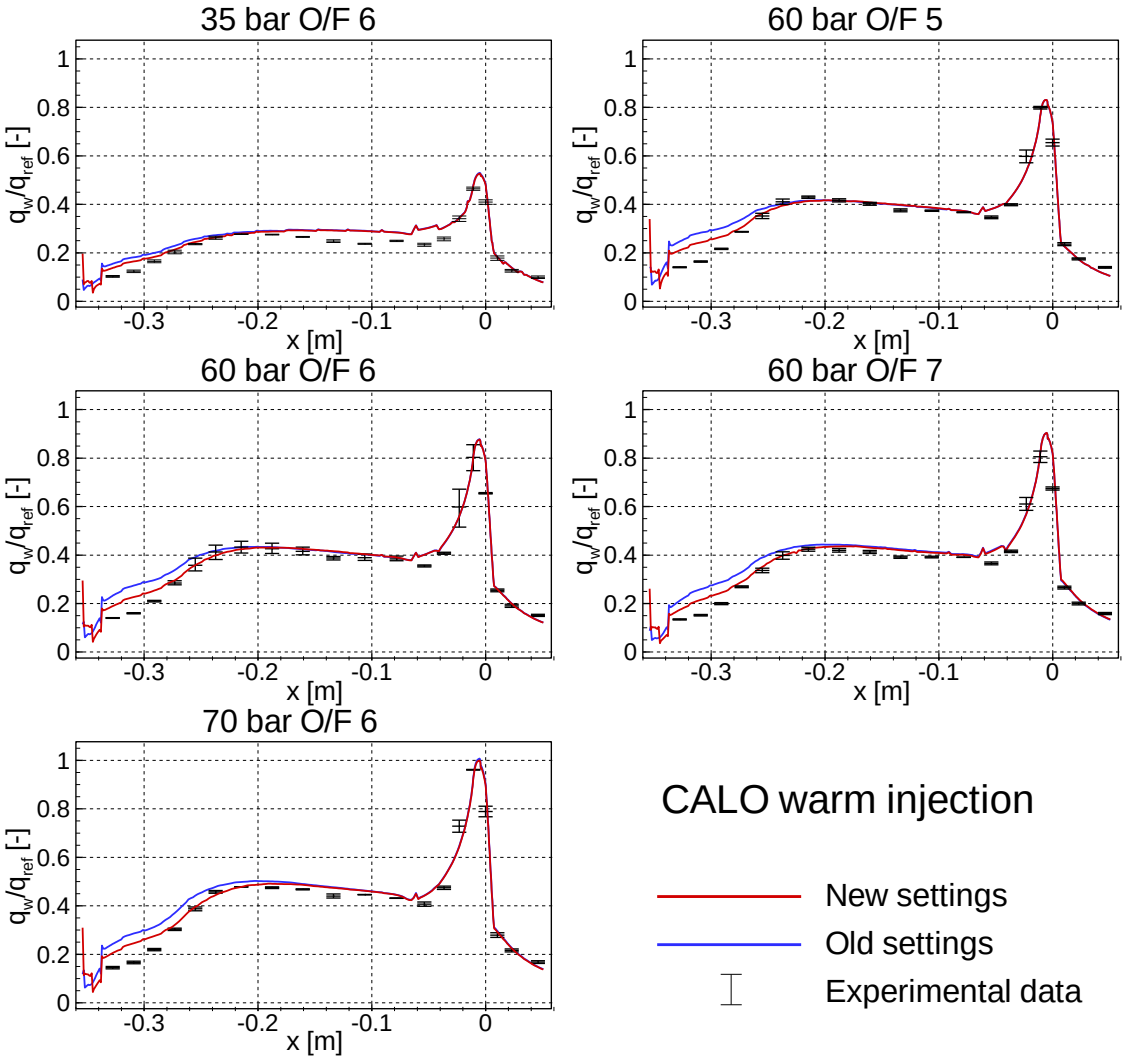

Figure 5.8: Wall heat flux $\dot{q}_w$ of the CALO test chamber load points with warm injection. The new and old settings are shown together with experimental data.

The new settings show a substantially better fit to the experimental data than the older ones in the first third of the chamber ($-0.33 < x < 0.2$). As for the cold injection load points the change is in the region very close to the faceplate ($x < -0.33$) due to an unaccounted change in the Rocflam-II source.

5.6 Full scale simulation Vulcain 2

A full scale simulation of the Vulcain 2 engine was performed to investigate the result of the Rocflam-II formulation change and the impact of the new lookup table. The Vulcain 2 is a H2/O2 cryogenic engine currently in use on the first stage of the Ariane 5 launch system. It provides 1350 kN of thrust with a nominal specific impulse of 434 s [**7**]. The engine is simulated at the M216-01-250s load point specified in Table 5.2.

Table 5.2: Parameters for the Vulcain 2 full scale M216-01-250s load point used in simulation.

Load point	p_c	O/F	$\dot{m}_{H2}$	$\dot{m}_{O2}$	$T_{H2,inj.}$	$T_{O2,inj.}$
M216-01-250s	124 bar	7.28	38.1 kg/s	277.8 kg/s	~100 K	~100 K

Typical contour plots of the temperature and O/F for the Vulcain 2 chamber are shown in Figure 5.9. The 13 rows of injection elements can be seen clearly in the lower figure with the central LOX streams causing the high O/F values close to the faceplate.

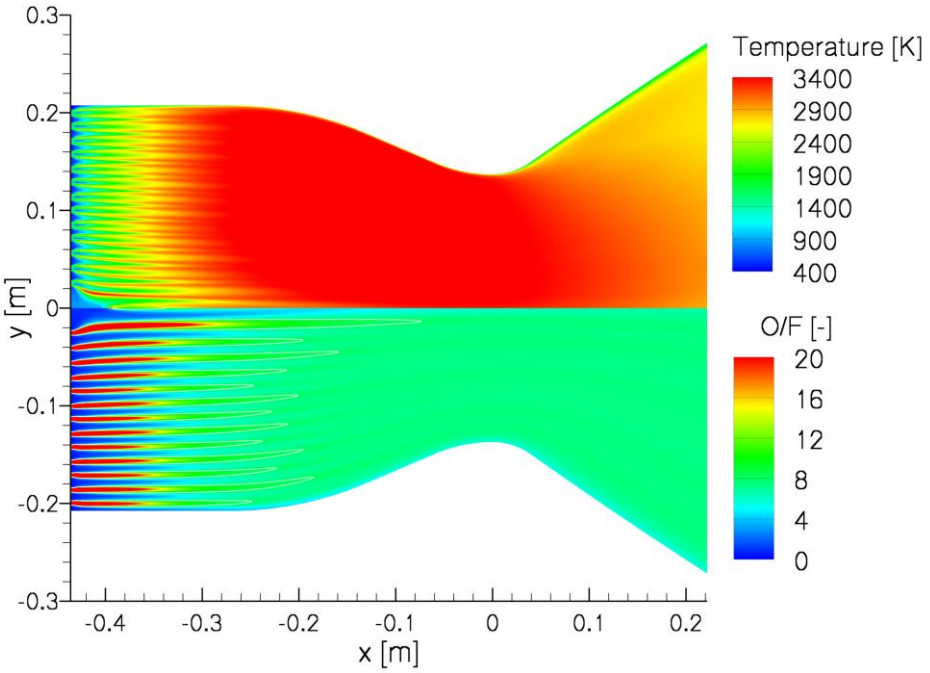

Figure 5.9: Contour plot for the temperature (top) and O/F (bottom) for the Vulcain 2 chamber in the M216-01-250s load point. The white lines in the lower plot indicate stoichiometry ($O/F = 7.937$)

For the Vulcain 2 engine no experimental data exists for the axial evolution of the specific wall heat flux. Instead the integral heat load is measured through the regenerative cooling system and used to compare the accuracy of the simulation. Another measure available is the pressure drop of the coolant dP between the start and end of the one dimensional pipe simulated by RCFS-II. There is also experimental data available for dP that can be compared with simulations. A typical progression of the coupling between the flow and combustion simulation to the RCFS-II module can be seen in Figure 5.10. The integral heat load and the pressure drops converge in a similar way to the specific wall heat flux and can be used to check on the convergence of the total system.

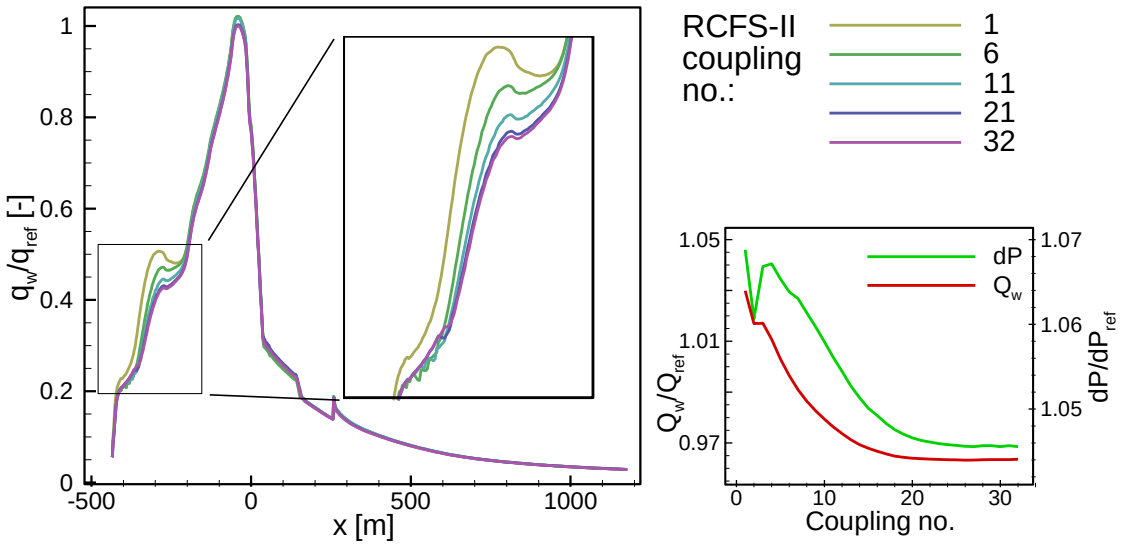

Figure 5.10: Progression of the specific wall heat flux $\dot{q}_w$ for a typical simulation of Vulcain 2 where a large change is made in the simulation conditions. The integral heat load $\dot{Q}_w$ and pressure drop dP converge in a similar way after approximately 30 couplings. The y-axes of $\dot{Q}_w$ and dP are each scaled with the measured experimental value (see Table 5.3 for final results).

The same Rocflam-II formulation change as described above was also performed for the Vulcain 2 simulation. Through the empirical formulas of [**11**] the two SMDs were estimated in the same way as for the CALO chamber to be 80.5 and 81 µm for the (2.9) respectively (2.10) formula. Because of the similar injection elements and injection temperatures of Vulcain 2 compared to the cold injection CALO chamber the cold correction function (see Figure 5.6) was applied as in (5.2) to produce the corrected MMD for the M216-01-250s load point.

$$\begin{aligned} \mathrm{MMD}_{\mathrm{corr}} &= 0.7079e^{0.1157\cdot 7.28}\left[\frac{1}{2}\left(SMD_{(2.9)} + SMD_{(2.10)}\right)e^{0.5\sigma^2}\right] \\ &= 135.5\ \mu\mathrm{m} \end{aligned} \tag{5.2}$$

In Figure 5.11 the two specific wall heat fluxes of the new and old Rocflam-II settings are compared for two Vulcain 2 simulations. The greatest differences are seen in the front part of the chamber with a maximum deviation of 2.1%. In Table 5.3 the integral heat load and the coolant pressure drop are compared to the experimental measurement of these variables. As seen in the figure the new and old settings are very similar with an under- respectively overestimation for the integral heat load and the pressure drop.

Table 5.3: The integral heat load $\dot{Q}_w$ and the pressure drop of the coolant dP for the new and old settings of the M216-01-250s Vulcain 2 load point compared to experimental data.

	Experiment	Old settings	New settings
$\dot{Q}_w/\dot{Q}_{ref-Vulcain2}$ [-]	1	0.9650	0.9637
$dP/dP_{ref-Vulcain2}$ [-]	1	1.0463	1.0456

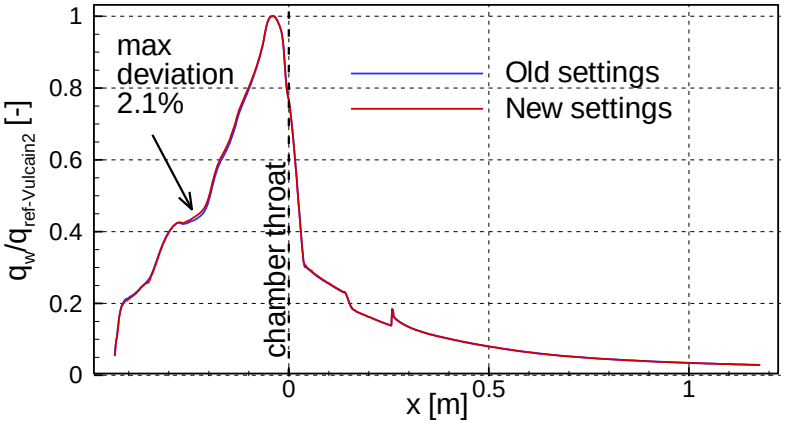

Figure 5.11: Specific heat flux $\dot{q}_w$ for the Vulcain 2 engine with the new and old settings applied. The greatest deviation of 2.1% is seen in the front part of the chamber at $x = -0.21\ m$.

5.7 Discussion

The results of the CALO simulations for both cold and warm injection show an overall good fit to the experimental data except in the front part of the chamber. Here one can assume that 3D effects dominate that cannot be described very well by the 2D grid. Notable is that the new settings describe this part significantly better than the previous settings for the warm injection which would indicate that the simulation has increased its accuracy in this region after the formulation change. The new settings for the Vulcain 2 simulation also show good agreement to the previous results. The changes to experimental values due to the new settings in Table 5.2 are not big enough to conclude regarding increase or decrease of simulation accuracy for this case.

The increase of the C_{diff} parameter translates to an increase of the droplet evaporation rate (see Figure 5.3). This incurred an adjustment of the droplet distribution to higher MMDs that has the effect of delaying the total vaporization by making the droplets bigger (see Figure 5.4). These two effects compensate each other to a large extent and keep the original vaporization distribution in the chamber.

The correction factors generated by the correction functions of the CALO test are exceptionally large indicating a spray with almost three times the MMD suggested from literature. Experiments made by Vingert et al. in [**11**] with LOX and gaseous nitrogen of the coaxial injectors in question indicated that water showed a similar spray distribution as the LOX. Vingert et al. also conclude that the measurements of the LOX tests could be flawed and that a smaller MMD is expected by the empirical relations found by the water tests. The contradiction of the simulation indicating a significantly larger MMD than the results from Vingert et al. is probably due to a combination of two factors.

The first factor arises in the conditions for the experiments performed by Vingert et al. Here the injector elements are only tested as a subsystem of the total combustion chamber. This has the effect that interactions between the different elements are neglected. Furthermore, the experiments are only performed with non-reacting propellants since the alternative would be very hard to measure. The effect of the propellants reacting and the resulting high temperature gas can therefore also not be measured experimentally. The high temperature gas formed in the shear layer between the two streams induces strong volume sources in the gas phase because of the great difference in density between the two phases. In Figure 5.12 a clear effect of this in simulation can be seen where the central LOX droplet stream is divided into three main branches because of the rapid expansion in the hot temperature zones where combustion takes place. This "break-up" effect of the spray can also not be measured in the experiment by Vingert et al.

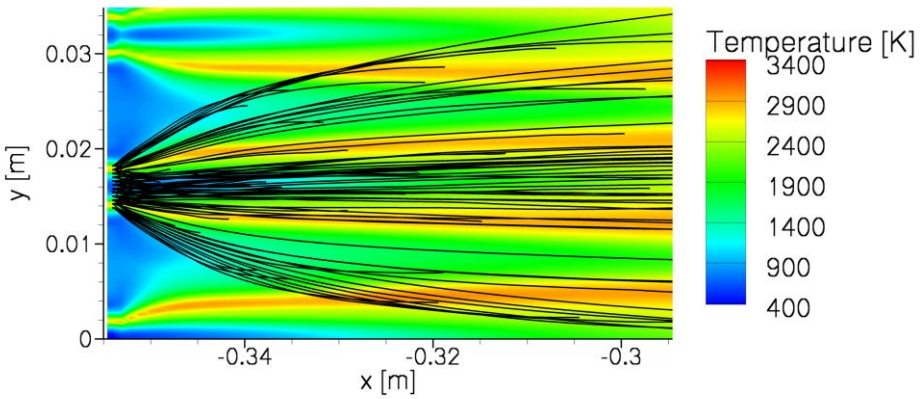

Figure 5.12: Droplet trajectories from the "middle" LOX injector element for the CALO 60-6 warm load point. The background shows the converged temperature distribution from the Navier-Stokes solver.

The second factor contributing to the large difference between experiment and predictions from simulation is the assumptions for the Rocflam-II Lagrange module.

One of these assumptions is the 2D approximation, omitting any three dimensional effects of the spray into the chamber. The droplet evaporation is also modeled with subcritical assumptions when they are in fact injected transcritical. Another assumption is the injection origin of the droplets. In reality the droplets are formed in the shear layer between the fuel and oxidizer stream as seen in Figure 2.2. In the simulation the droplets are injected at the base of the flame leading to other conditions for the trajectories simulated by the Lagrange module.

Judging by the multiple flaws in the experiment conditions and the simulation assumptions we can assume that the correction factors are not unrealistic for the presented combustion chambers and can be used for approximating droplet distributions for other H2/O2 chambers.

6 Conclusion

In the frame of this master's thesis a new parameter setting for simulating H2/O2 rocket thrust chamber in Rocflam-II has been found together with implementation of changes to the program generating the equilibrium lookup tables (CEA2FHR).

The new version of the table generation program for Rocflam-II developed for Methane-LOX fuel combinations in [**4**] was validated against an older version for the H2/O2 application. After program modifications (see Appendix A) the new H2/O2 lookup table was found to have two major differences to the previous table. One of these consists in a temperature change of about 20 K in the fill-up region and a slight cooling (max. 10 K) for high temperatures close to the stoichiometric mixture fraction (see Figure 3.1). The second major difference consists of a slight discontinuity in the density computed close to the phase transition between liquid and solid water in the table (see Figure 3.2). Future work could remove the discontinuity by expanding the implemented low temperature correction to the entire region containing condensed phase. Simulation results (see Section 3.1.1) showed no significant difference between the new and old lookup table for the CALO and Vinci subscale thrust chambers.

The table generation program was also altered to generalize the number of reaction products available in the table (see Section 3.3). By either connecting directly to the common blocks or modifying the source code of the CEA subroutine the former limitation of 12 species was lifted. For a typical Kerosene-GOX table the modification resulted in small changes to the mass fraction proportions and a slight influence on the heat capacity (see Figure 3.4). The envisaged increase in computational efficiency associated with the common block connection as assumed in the introduction was not reached (see Table 3.2). Instead the low temperature subroutine *stoffdaten.f* was identified to be the most effective target for increasing efficiency (see Section 3.2.1).

A value for the isothermal compressibility for multi-phase mixtures was implemented in the table replacing the former ideal gas approximation (see Equation (2.28) respectively (2.21)). The new calculations resulted in a higher compressibility for the multi-phase than the former approximation due to the gas no longer being approximated to make up all of the mass (see Figure 3.6). The change to the table compressibility coefficient C_ρ was shown to have a negligible influence on the simulation results (see Figure 3.7),

since it enters the simulation only as a correction term and should ideally be zero at convergence (see Section 2.2.4).

A study of the lookup table resolution influence to simulation results was performed using the Vinci subscale chamber as a test case. The study showed upon overall sufficiently high default resolution values with a weak link between precision of simulation indicators and table resolution (see Figure 4.3). A possibility to increase precision by approximately 0.5‰ for three of the four indicators was identified and realized by shifting resolution of the mixture fraction dimension from the oxidizer rich to the fuel rich side (see Section 4.3).

A new formulation in the Lagrange module of the Rocflam-II source and new value of the diffusion coefficient C_{diff} were implemented for simulating H2/O2 thrust chambers (see Section 5.2). The changes resulted in an increased consistency between how different propellants were treated in the diffusive transport between the droplets and the gas phase. New correction functions (see Figure 5.6) for the droplet distribution were found using the CALO test case. By optimizing the droplet distribution MMD to correctly predict the experimental results a relationship between the correction factor and the oxidizer to fuel ratio O/F could be found. The new correction functions show a poorer agreement to the experimental results by Vingert et al [**11**] than before the formulation change. The fit to the experimental data was for both cold and warm injection of the CALO chamber very similar to the previously simulated results, except for warm injection where a small trend towards better fits in the first third of the chamber could be seen (see Figure 5.7 and Figure 5.8). The correction functions together with the new formulation was later applied to simulation of the full scale Vulcain 2 thrust chamber with good agreement to the result with the older settings (see Figure 5.11).

In conclusion the presented work has increased the consistency of the Rocflam-II CFD tool for simulation of H2/O2 rocket thrust chambers. It has also increased consistency of the lookup table generation software, CEA2FHR, between different fuel mixtures. The global accuracy of the Rocflam-II simulations has, through the optimization of the table resolution and changes to the Rocflam-II injection routine, increased.

References

[1] European Space Agency. (2012, February) Information kit ATV Edoardo Amaldi. Document. [Online]. http://download.esa.int/docs/ATV/Information_kit_ATV-3_FINAL.pdf

[2] European Space Agency. (2012, March) Ariane 5 ES. [Online]. http://www.esa.int/SPECIALS/Launcers_Access_to_Space/SEM20W67ESD_0.html

[3] Josef Görgen, Thomas Aichner, and Manuel Frey, "Spray Combustion and Heat Transfer Modelling in LOX/H2, LOX/HC and MMH/NTO Combustion Chamber," in *3rd European Conference for Aerospace Siences, EUCASS 2009-104*, Versailles, France, 6-9 July 2009.

[4] Martin Merkle, "Simulation of flow and combustion in gas generators taking into account low temperature," Mehanical and Process Engineering Technische Universität Darmstadt, Darmstadt, Master's Thesis 2011.

[5] Aichner Thomas, "Untersuchung des heissgasseitigen Wärmeübergangs in H2/O2 Raketenbrennkammern und -Düsen," Luft und Raumfahrt TU München, München, Diplomarbeit 2007.

[6] Benedikt Laub, "Berechnung der Strömung und Verbrennung in Raketenbrennkammern mit Hilfe eines 2D Navier-Stokes-Verfahrens," Technische Universität Kaiserslautern, Kaiserslautern, Diplomarbeit 2010.

[7] G Hagemann, O Knab, and Kau H-P, Course material "Raumfahrtsantriebe I/II", 2009, Technische Universität München Lehrstuhl für Flugantriebe.

[8] Stephanie Zawadzki, "Untersuchungen zur Tröpfchenverteilung in Raketenbrennkammern," Technische Universität München, München, Diplomarbeit 2008.

[9] Martin Seidl, "Zweidimensionale Berechnung der Strömmung und Verbrennung in H2/O2-Raketenschubkammern mit Hilfe eines Dense-Gas-Ansatzes,"

Insitute for Flight Propulsion, Technischen Universität München, München, Diplomarbeit 2011.

[10] Dag Wennerberg, Josef Görgen, Björn Kniesner, and Manuel Frey, "Technical Manual: Rocflam-II," EADS Astrium TP24, Ottobrunn, Manual 2008.

[11] L Vingert, P Gicquel, D Lourme, and L Menoret, "Coaxial Injector Atomization," in *Liquid Rocket Engine Combustion Instability*, Paul Zarchan, Ed. Washington, United States of America: American Institute of Aeronautics and Astronautics, Inc., 1995, vol. 169, ch. 6, pp. 145-189.

[12] Versteeg H K and Malalasekera W, *An introduction to computational fluid dynamics The finite volume method*. Harlow, England: Pearson, 1995.

[13] Joel H Ferziger and Milovan Peric, *Computational Methods for Fluid Dynamics*, 3rd ed. New York: Springer, 2002.

[14] Sanford Gordon and Bonnie J. McBride, "Computer Program for Calculation of Complex Chemical Equilibrium Composition and Applications," National Aeronautics and Space Administration, Cleveland, Ohio, Reference Publication RP-1311, 1994.

[15] Horizon Technologies. (2011, December) GASPAK Specifications. [Online]. http://www.htess.com/gaspak.htm

[16] Arnold Frohn, *Einführung in die Technische Thermodynamik,* 2nd ed. Wiesbaden, Germany: Aula-Verlag GmbH, 1989.

[17] Benedikt Laub, "Berechnung der Strömung und Verbrennung in H2/O2 - Raketenbrennkammern mit Hilfe eines 2D Navier-Stokes-Verfahrens," Astrium GmbH, München, Praktikumsbericht TP24-TN-72/2010, 2010.

[18] EADS Astrium. (2012, March) Vinci Rocket Engine - Thrust Chamber. [Online]. http://cs.astrium.edas.net/sp/launcher-propulsion/rocket-engines/vinci-rocket-engine.html

A Change list for CEA2FHR

A.1 Changes to cea2fhr.f

cea2fhr-20110929-plot.f

- Added option to read directly from common block of CEA. Controlled by parameter *CEACmnBlckRead*.
- Added option to turn off/on "real" dp/drho in the table. Controlled by parameter *RealDPDRHO*.
- Changed back to fix temperature (444 K) of starting temperature "guess" for *hp* problem in CEA input file (cea.inp)
- Other treatment of string for recognizing when a "pure" species is treated. Needed for other fuel combinations besides H2/O2.
- Included new modified CEA version (cea2_multisp.f) to handle fuel combinations were more than 12 species are needed.

cea2fhr-2012.f

A.2 Changes to stoffdaten.f

stoffdaten-20110929.f

- Changed minimum allowed temperature (to 60K) for the pure H2 case to avoid inconsistency in the table by losing mixed solution where the solution has a temperature under 60K.
- Set watersteam's dpdrho to the ideal gas approximation (RT) when used GASPAK routine failed to converge for low(?/some) partial pressures.
- Changed the way Cp is computed to avoid non-converging GASPAK points but mainly to have consistency with my and lambda that were already switched to be computed with an GWATER call instead.
- In case *sat_kond* changed to compute values of the other gaseous species with the partial pressure were the saturation of the steam has been accounted for (*p_part_sat*).
- Changed faulty drhodp mixing rule for gaseous species to correct one (now weighted by psi).
- Introduced protection of *drhodp_gas* variable summation to avoid division by zero overflows.
- In *sat_kond* changed to compute steam dpdrho (*dpdrho_H2O)* with same input as the GWATER call.
- Changed mixing rule in *sat_kond* for Cp to make it more transparent.
- Increased convergence limit for *unge_utr* (?) in entropy loop to have better convergence.
- Manually initialised *V_spez_gas* and *V_spez_fl* to avoid compilation(?) bug in computing corrected density in *sat_fest* case.
- Included support for **one** condensed non-water species in dpdrho mixing rule in *sat_fest* case. This to avoid bug where only condensed species existed in mixture (condensed O2 and H2O)

stoffdaten-20111214.f

- Uncommented the "bricolage" to avoid non-converging GASPAK of H2O for low pressures. This solved dip in temperature and density graphs.

stoffdaten-20120119.f

Changes to the *sat_fest* case:

- Changed calculation of the specific volume of the gas (*V_spez_gas*) to be computed as a sum of all the remaining gases. Former solution only computing for one gas.
- Added summation of the water gas phase density, specific volume and drhodp to the total gas values. Earlier this was not taking into account but neglected.
- Added coefficient *xEA* to calculation of specific volume of condensed water phase (*V_spez_fl*). Earlier it summed the entire H2O part to this. It is now divided between the gas and solid phase.
- Adjusted density calculation to ignore the gas phase where the condensed mass fraction (*massfr_liquid*) is calculated to be a tiny bit above one. Without this adjustment there was a chance of giving negative densities to the output table for very low temperature state points.
- Moved density limit for calculation of all-condensed drhodp values. For very low density values (~1E-10) the formula returns a very very high value of drhodp despite the state being "full" with condensed species. This was primarily caused by the tiny bit of H2O gas computed from the linear formulas for the water gas phase.

stoffdaten-201202.f

A.3 Changes to cea2.f

cea2.f

- Increased the number of possible species that can be plotted in one row in the plt-file
  - Changed common blocks definitions from cea.inc to cea_multisp.inc, where in the latter the size of Pltvar is 50 instead of 20.
  - 234; 243: Changed format dimension from 20 to 50 (number of variables to plot in one row)
  - 2227: Changed processing of OUTP dataset (from 20 to 50 allowed variables).

cea2_multisp.f

/Erik Larsson, master thesis worker, Astrium TP24, October 2011 – March 2012